Experimental Investigation of Lunar Prototype Wheel Traction Performance on Deformable Terrain

By

Nasim Kaveh-Moghaddam

Department of Mechanical Engineering

McGill University

Montreal

February, 2011

A Thesis submitted to the Faculty of Graduate Studies in partial

fulfillment of the degree of Master of Engineering

i

Abstract

Travelling long distances with maximum reliability are necessary requirements for future lunar rover missions. Rovers' mobility performance highly depends on wheel type and the mechanical properties of the terrain on which it is rolling. On the lunar surface, the terrain is primarily composed of very fine grained abrasive particles called regolith. Traditional pneumatic rubber wheels are not a viable option for planetary rovers, due to the unknown properties of rubber over a long term exposure to radiation, and the chances of failure in the near vacuum environment. Therefore, non-pneumatic non-rubber compliant wheels have been recognized as a best possible option for planetary exploration rovers.

The present research thesis focuses on testing procedures and data analysis of different prototype wheels, rolling on dry sand, by considering several wheel-soil performance parameters including traction, slope climbing ability, rolling resistance, and power consumption. Results from these experiments demonstrate some of the main wheel properties that can affect wheel performance at low speed conditions and provide preliminary data for validation of wheel-terrain model simulation performed within the McGill University research group. The tested wheels were designed and tested at McGill University, Montreal, Canada, as part of a partnership program between the Canadian Space Agency, Neptec Design Group and a number of associated organizations.

Résumé

Traverser des longues distances avec un maximum de fiabilité sont des conditions nécessaires pour les futures missions des véhicules d'exploration lunaire. La mobilité des "rovers" d'exploration planétaire dépend extrêmement du type de roue et des propriétés mécaniques du terrain sur lequel elle roule. Sur la surface lunaire, le terrain est principalement composé des grains abrasives très fins, appelé "regolith". Les roues pneumatiques traditionnelles ne sont pas une option viable pour les "rovers" d'exploration planétaire, en raison des propriétés inconnues de caoutchouc sur une exposition à long terme au rayonnement, et les hasards d'échec dans le vide.

Ce projet de recherche se concentre sur les procédures d'essai et d'analyse des données des différentes roues prototypes roulant sur un terrain déformable, en mesurant plusieurs paramètres de performance y compris la traction, la capacité de monter des pentes, la consommation de pouvoir et la résistance au mouvement de roue sur le sable sec. Les résultats de ces expériences démontrent certaines propriétés de roue qui peuvent affecter la performance de roue roulant à basse vitesse sur le sable sec et fournissent des données préliminaires pour la validation des simulations de modèles de roue sur terrain déformable qui ont été faites parmi le groupe de recherche à l'université McGill Montréal, Canada. Les roues prototypes ont été conçues et testées à l'université McGill, dans le cadre d'un programme de partenariat entre l'Agence Spatiale Canadienne, Neptec Design Group et un nombre d'organisations associées.

Acknowledgements

This research would not have been feasible without the help and constant support of many people. First, I would like to thank my research supervisor, Professor Peter Radziszewski for providing me this amazing opportunity to work on such an interesting subject that was related to the planetary exploration rovers. His constant guidance, support and positive attitude throughout the course of this project were invaluable and helped me to gain knowledge of the research and achieve successful experimental results.

I gratefully acknowledge Professor Ferri Hassani from the Department of Mining Engineering and the mining laboratory students and their invaluable feedbacks. I am indebted to the help and assistance of my colleagues: Mr. Sudarshan Martins and Mr. Michele Faragalli for their constant support and feedbacks for the experiments and the thesis manuscripts, and Mr.Nima Gharib, Mr. Robin Briend, Mr. Amar Sabih and Mr. Jean-Philippe Lafleur for their assistance for the experiments. I am also grateful to the help and technical assistance of our technicians Mr. Georges Tewfik, Mario Iacobaccio, and Gary Savard. I would like to thank the Canadian Space Agency, for providing the working environment to complete the single wheel testbed experiments. I am thankful to Mr. Alessio Salerno for his day to day presence to give me access to the facility and his helpful feedbacks for the experiments.

I would like to express my love to my family for the unconditional support and endless love and encouragement.

Table of Contents

Chapter 1

Introduction

1.1 Problem Statement and Motivation
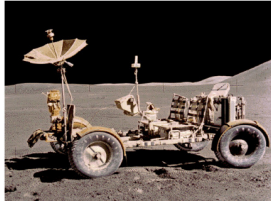
Space exploration has been a source of inspiration and a challenge for both science and technology. In the field of planetary exploration, the use of robotic rovers has been a great asset in the accomplishment of high-risk missions and in the expansion of the exploration area (Wong J. , 2010).

Rovers' mobility performance highly depends on wheel design and the mechanical properties of the terrain on which it is rolling. On the lunar surface, for example, the terrain is primarily composed of very fine grained abrasive particles called regolith. Traditional pneumatic rubber wheels are not a viable option for planetary rovers, due to the unknown properties of rubber over a long term exposure to radiation, and the chances of failure in the near vacuum environment (Asnani, 2009). Therefore, non-pneumatic non-rubber compliant wheels have been recognized for planetary exploration rovers (Faragalli, et al., 2010). Similarly, an understanding of the effect of wheel's parameters, such as size, shape and flexibility, on off-road vehicle mobility performance through physical testing of wheel prototypes and modeling of the wheel-soil interaction is essential to create efficient wheels by considering the developed thrust and rolling resistance, bearing load capabilities and wheel velocity in planetary exploration missions.

For lunar exploration, two types of rovers and a push cart have been used, for different lunar missions, dating from 1970 to 1973 (see Fig. 1.1). An important investigation for off-road vehicles was made during Apollo 15 program, under the

guidance of Dr M.G. Bekker. Apollo 15 was the forth mission to land men on the Moon and was the first mission to carry a Lunar Rover Vehicle (LRV), which allowed the astronauts to travel much further from their landing site and sample a much wider variety of lunar materials than the other lunar missions (Costes, Farmer, & George, 1972). A number of different prototype wheels were investigated through extensive physical testing in order to determine the ideal wheel for the given mission. The wire-mesh compliant wheel design for the LRV rover was recognized as the best option for the Apollo mission.

According to Asnani, et al., (2009), the lunar rovers of the 1970's and their respective wheels, as illustrated in Fig. 1.2, were designed for short duration missions, small distances, low velocities, and they were limited in their capacity to transport heavy loads.

Rover:	**Lunokhod**	**MET**	**LRV**
Missions:	Luna 17, 1970	Apollo 14, 1971	Apollo 15, 1971
	Luna 21, 1973		Apollo 16, 1972
			Apollo 17, 1972
Max speed:	2 km/hr	~4 km/hr	16 km/hr
Max distance	37 km	~3 km	36 km
Max load:	~800 kg	~75 kg	~700 kg

Fig. 1.1: Rovers used in lunar exploration missions (Asnani, 2009)

Lunokhod	MET	LRV
Rigid, wire carcass connected by spokes	Rubber carcass supported by nitrogen filled inner tube (10.3 kPa)	Flexible, wire-mesh carcass and stiff inner frame
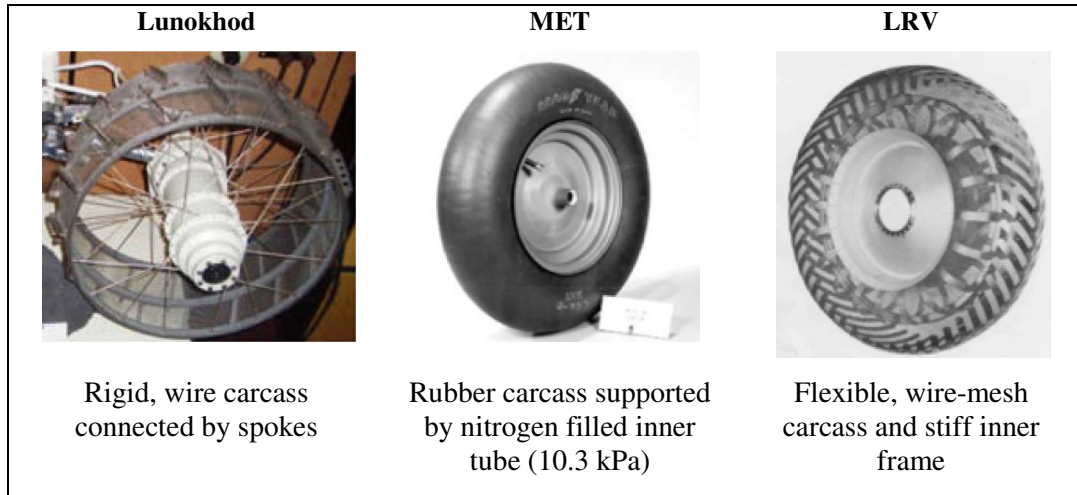
Fig. 1.2: Wheels used in lunar rovers (Asnani, 2009)

Even though, the wire-mesh compliant wheel was the best design for the LRV mission, nevertheless, it cannot satisfy the future lunar mission objectives and performance requirements. Lunar missions' requirements have been evolved since 1970's (Faragalli, et al., 2010). Future lunar and planetary rovers will require a new generation of wheels that can operate for longer durations, with higher tractive capabilities and an increased load capacity (Wong, 2010; Asnani, 2009; Iagnemma & Dubowsky, 2004). Rovers will travel longer distances on the lunar surface, and perform large number of tasks such as transport sensitive payloads, and be assigned for operations with or without human assistance (Faragalli, et al., 2010). Some of the preliminary mobility performance metrics for future lunar rovers and wheels are classified in Faragalli, et al., (2010).

Lately, two new non-rubber non-pneumatic compliant prototype wheels have been made and tested by Michelin and Goodyear Tire Company for terrestrial use and potential planetary rover missions (Faragalli, et al., 2010). In

Canada, the Canadian Space Agency has initiated studies on the development of concepts and technologies in support of lunar mobility systems development. One study, led by the Neptec Design Group, aims to investigate, conceptually design and test a lunar mobility system (Radziszewski, et al., 2010). The objective of this thesis project is to outline the testing procedures and present the experimental results of the traction performance of several prototype wheels, designed at McGill University, as part of this partnership program. The following section provides the main objectives of the present research.

1.2 Purpose of the Thesis

The purpose of this thesis is to experimentally investigate the effect of several prototype wheels' parameters on tractive performance while rolling in straight-line motion on deformable soil at different operating conditions. In doing so, preliminary data for the validation of simulated wheel-terrain interaction models, as outlined by (Briend, et al., 2010; Faragalli, et al., 2010; Gharib, et al., 2010), is obtained.

Wheel parameters are related to the physical geometry and dimensions of each wheel. Wheel tractive performance theory will be reviewed in chapter 2. The specific objectives of this project are as follow:

1. Review the basic theory of rigid wheel-deformable terrain interaction based on Bekker and Wong's models and the experimental background in determining the wheel performance metrics such as wheel drawbar pull, slope climbing ability, overall motion resistance, and power consumption.

2. Describe the prototype wheels and explain the experimental apparatus, and the testing procedures for evaluation of their performance.

3. Experimentally investigate the prototype wheels traction performance and soil mechanical properties such as the internal friction angle and soil cohesion. Tractive performance was evaluated in terms of drawbar pull, hill climbing angle, power consumption, and coefficient of rolling resistance in straight line motion at constant velocity. The drawbar pull and hill climbing angle were measured at 100% wheel slip at varying normal loads; whereas power consumption and coefficient of rolling resistance were evaluated at very low slip and low velocities with varying normal loads.

4. Comparison of experimental drawbar pulls with Bekker and Wong rigid wheel-deformable terrain interaction models.

1.3 Thesis Outline

This thesis is composed of five chapters and one appendix. This chapter serves as an introduction and presents the motivation and objective of the project. Chapter 2 covers the literature review. More specifically it explains the theory of rigid wheel-deformable terrain interaction and highlights the experimental methods to determine wheel performance metrics. Chapter 3 presents the prototype wheels and describes the testing procedures, and testing schemes for evaluation of their performance. Chapter 4 shows the experimental results through graphs and tables and discusses the different wheels performance metrics.

Furthermore, Chapter 4 verifies the analytical drawbar pull from Bekker and Wong's rigid wheel-deformable terrain models and compares the analytical models with the experimental results. Chapter 5 concludes the research paper and gives recommendations for further improvements of prototype wheels design and testing methodologies.

Chapter 2

Background and Literature Review

This chapter reviews the basic theory of rigid wheel-deformable terrain interaction based on Bekker and Wong's models. More specifically, it explains the semi-empirical equations developed by Bekker and Wong to determine one of the most important wheel performance parameters, the drawbar pull which defines the force available to the wheel for overcoming the resistances to motion and to move the wheel forward. Furthermore, this chapter explains the experimental approach in determining the wheel performance metrics, such as wheel drawbar pull, slope climbing ability, overall motion resistance, and power consumption.

2.1 Wheel-Terrain Interaction Classifications

In general, wheels are classified as rigid or deformable based on their degree of deflection under static loading. Rigid wheels have a constant diameter or deflections less than 10% of the diameter, such as hard metallic wheels and pneumatic tires with an inflation pressure higher than the terrain stiffness. Flexible wheels deflect 10% and more of the rolling diameter; they could be made by thin wall metallic or non-metallic materials to provide the necessary elasticity properties, and low-to medium-pressure pneumatic tires (Apostolopoulos, 2001). Similarly, the surfaces on which wheels traverse are also classified as rigid or deformable. As a result, wheel-terrain interaction models are grouped in four different cases, as illustrated in Fig. 2.1 (Iagnemma and Dubowsky, 2004).

a) Rigid wheel-rigid terrain

b) Deformable wheel-rigid terrain

c) Rigid wheel-deformable terrain

d) Deformable wheel-deformable terrain
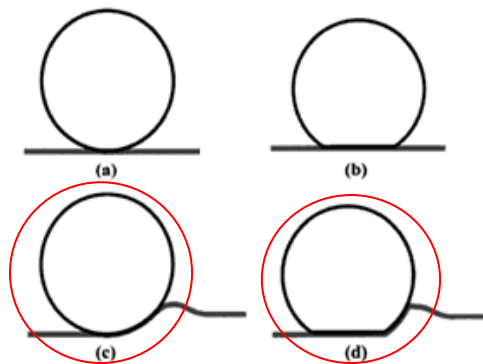
Fig. 2.1: Four cases of wheel-terrain interaction models (Iagnemma & Dubowsky, 2004)

Cases (a) and (b) define the on-road mobility system, whereas cases (c) and (d) describe the off-road mobility structure. A more detail explanation of each system can be found in Iagnemma and Dubowsky (2004). Here, the focus is on the experimental analysis of rigid and deformable wheels rolling on soft terrain (cases (c) and (d) in Fig. 2.1) and theoretical evaluation of rigid wheel-soft terrain model (case (c) in Fig. 2.1).

2.2 Rigid Wheel-Deformable Terrain Interaction Models

The traction performance of a wheel, in straight line motion, refers to its ability to overcome motion resistances, to develop drawbar pull, to negotiate slopes, or to accelerate (Wong J. , 2010). Fig. 2.2 gives the external forces, stresses and wheel-soil parameters of a driven rigid wheel moving at constant velocity, V, in straight-line motion on deformable terrain (Wong, 2010). As shown in Fig. 2.2, when a torque, T, is applied to a rigid wheel under certain applied vertical load, W, a tangential (shear) force, τ, develops at the soil-wheel interface. At the same time, the vertical load causes a radial stress distribution, σ, beneath the wheel, at the soil-wheel interface. The soil-wheel interface is the surface of the wheel which is in contact with soil and is identified by the angle θ; from an exit angle, θ_2, to an entry angle, θ_1.
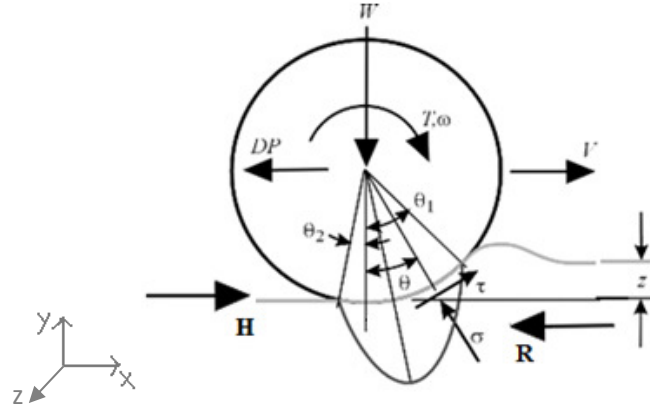
Fig. 2.2: Forces, torque and stresses acting on a driven rigid wheel (Wong & Reece, 1967)

At zero acceleration, which is the case presented here, the summation of the external forces in the x-direction, as defined in Fig. 2.2, is given by equation 2.1 (Laughery, Gerhart, & Goetz, 1990):

$$H - DP - R = 0$$

$$DP = H - R$$

(2.1)

where

H   is the effective thrust or gross tractive effort

DP   is the drawbar pull, or net tractive effort

R   is the translational rolling resistance

The drawbar pull (DP) is one of the most important parameters in the evaluation of the performance of the wheel, as it defines the force available to wheel for overcoming the resistances to motion (R) and to move the wheel forward. Therefore, the selection of an optimum wheel is based on its capability to maximize soil thrust while minimizing motion resistance. Maximizing drawbar

pull also improves the slope and obstacle climbing abilities (Apostolopoulos, 2001).

There exist different methods in predicting the wheel traction performance on soft terrain. In Tiwari, et al. (2010), the traction prediction models have been reviewed and grouped under three different approach types: (1) Analytical approach, (2) Empirical approach, and (3) Semi-empirical approach. In analytical model (1), the wheel traction performance is predicted by defining the distribution of normal and shear stress at the soil-wheel interface and the geometry of the 3-D contact surface theoretically. Finite element models (FEM) or discrete (distinct) element method (DEM) or a combination of both are particularly used to investigate the complex geometry and soil and wheel material nonlinearities. However, predicting wheel traction analytically is known to be very complex, because of the inadequate knowledge of boundary conditions and numerous soil parameters. The empirical approach (2) is used for quick numerical evaluation of soil in the field, and it is based on soil-cone index as the only soil strength parameter. In this method, the traction performance is predicted by dimensionless relationships that use different wheel mobility numbers found for specific types of terrains and valid for specific wheel geometry situations. Therefore, for a given traction test, if the wheel geometry, testing environment and soil properties do not match with previously found empirical equations conditions, then new empirical equations need to be developed. The semi-empirical approach (3) uses both wheel-terrain theoretical model and experimental soil properties to predict the traction performance. Two different analog devices are used to measure two types of soil geotechnical properties: a) soil pressure-sinkage coefficients, and b)

soil shear-stress parameters. In this chapter, Wong and Bekker's semi-empirical approach are presented, and experimental methods to determine the two soil properties are described. Bekker's model, as outlined by (Patel, et al., 2004; Wilkinson & DeGennaro, 2007; Radziszewski, et al., 2009), and Wong's model as developed by Wong and Reece (1967) have been adopted to compare the experimental drawbar pull in this research.

2.2.1 Wong's Model to evaluate Drawbar Pull

In Wong's model, each of the terms in equation (2.1) is evaluated by the summation of internal forces produced by the radial and tangential stresses beneath the wheel as described by equation (2.2). Radial stress is the ratio between the normal force to the surface and the area normal to the surface, whereas the shear stress is the ratio of tangential force, which is parallel to the soil surface, and the area normal to the surface. Therefore, internal forces in horizontal and vertical directions could be evaluated by the product of each of the stress components with their surface area. For example, for an infinitesimal section of the wheel in Fig. 2.2, the surface area is the product of the wheel width, b, in z-direction, by r.dθ. Therefore, the drawbar pull could be evaluated by integrating the product of horizontal components of the average tangential stress and radial stress with the infinitesimal wheel contact patch along the soil-wheel interface, as described by the following equation (Wong, 2010):

$$DP = rb\left\{\int_{\theta_2}^{\theta_1}\tau(\theta)cos\theta d\theta - \int_{\theta_2}^{\theta_1}\sigma(\theta)sin\theta d\theta\right\} \qquad (2.2)$$

The first term in equation (2.2) is the effective thrust, H, developed by the shearing action of the wheel and the second term which is in negative x-direction represents the rolling resistance, R, which is caused by the x components of normal stress. In order to develop expressions for the shear and radial stress, one could separate the wheel model into two components: horizontal and vertical deformations in the soil-wheel interaction as illustrated in Fig. 2.3. As a result of this model approach, the soil can be described by means of two characteristics: shear stress distributions and normal pressure distributions. These two components are both functions of soil mechanical properties and wheel geometry under wheel loading (Wong, 2010).
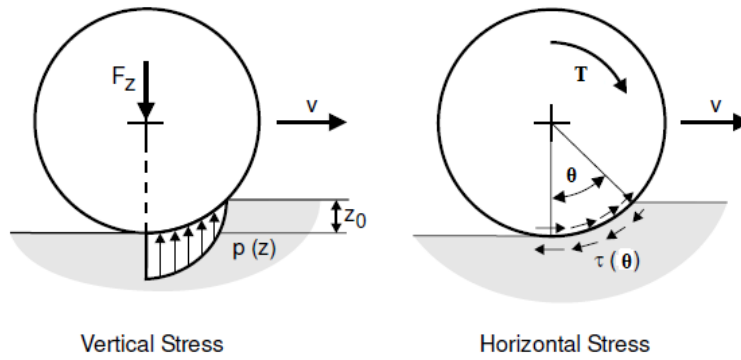
Fig. 2.3: Separation of vertical and horizontal stress in wheel-soil model (Matlab/Simulink, User's Guide, 2003, 2005)

Section 2.2.2 will identify the expressions for the shear stress distribution beneath the wheel responsible for wheel thrust and section 2.2.3 will explain the normal stress developed beneath the wheel causing wheel sinkage and resistance to wheel motion. Section 2.3 will cover some of the experimental techniques to measure

14

wheel performance metrics such as the drawbar pull, wheel slip and slope climbing ability.

2.2.2 Terrain Characteristics: Shear Stress Distribution

Fig. 2.4 shows the stress-strain relationship of an idealized elastoplastic material. Certain types of terrains, such as saturated clay and compact sand, have the same trend as the elastoplastic material under a given applied load. Usually, if the stress level in the terrain does not exceed a certain limit, as denoted by point A in Fig. 2.4, the terrain behaves as an elastic material. However, at stress levels beyond point A, the strain increases rapidly and the material falls in plastic flow region, shown by region A-B. The transition from plastic equilibrium, point A, to that of plastic flow represents the failure of the mass (Wong J. , 2010).
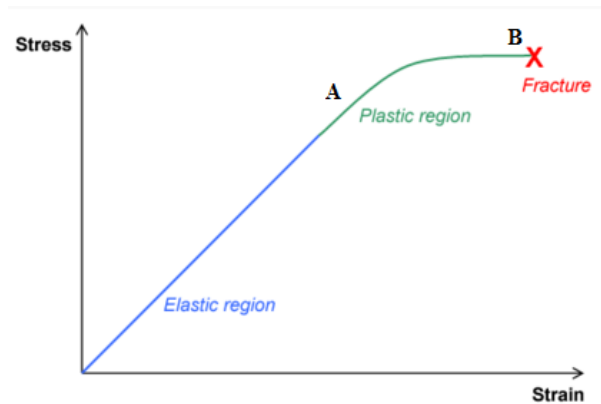
Fig. 2.4: Stress-strain relationship of an idealized elastoplastic material

In this study, the focus is on plastic theory of wheel-terrain interaction model that was conceived by Wong and Bekker. One of the most common criteria proposed for the failure of soils is the Mohr-Coulomb criterion. It proposes that the material will fail at a point if the shear stress at that point follows the condition:

$$\tau_{max} = c + \sigma tan\varphi \tag{2.3}$$

τ_{max} is the maximum shear strength of the material, c is the apparent cohesion of the material, σ is the normal stress on the sheared surface, and φ is the angle of internal friction of the material. The values for c and φ are experimentally found using different techniques such as triaxial or direct shear tests. The experimental approach to measure the soil geotechnical properties using direct shear test is covered in Chapter 3, section 3.4.

Based on the Mohr-Coulomb criterion, Bekker has developed the general ideal thrust for a vehicle with a wheel-soil contact area of A, per wheel, and no grousers as follow (Laughery, Gerhart, & Goetz, 1990):

$$H_0 = Ac + \frac{W}{n} tan\varphi \tag{2.4}$$

n is the number of wheel.

Contact area is the product of wheel width (b) and wheel contact length (L). The contact length (L) can be found using wheel geometry shown in Fig. 2.5, with a wheel diameter of (d) and sinkage (z) (Radziszewski, et al., 2009):

$$L = \sqrt{d^2 - (d - 2z)^2} \tag{2.5}$$

Where sinkage (z) for 1 wheel is expressed as follows:

$$z = \left(\frac{3W}{(3-n)k.b\sqrt{d}}\right)^{\frac{2}{(2n+1)}}$$

The expression of thrust in equation (2.4) developed by Bekker is function of wheel's contact area, wheel load and soil properties (c and φ). As can be seen from that equation, the ideal thrust increases with wheel load and contact area. If,

the soil is cohesive, then its internal friction angle is smaller, therefore, the contact area (A), has a bigger impact on the ideal thrust. However, if the soil is dry sand, with no cohesion (or c=0), which is the case in the present study as
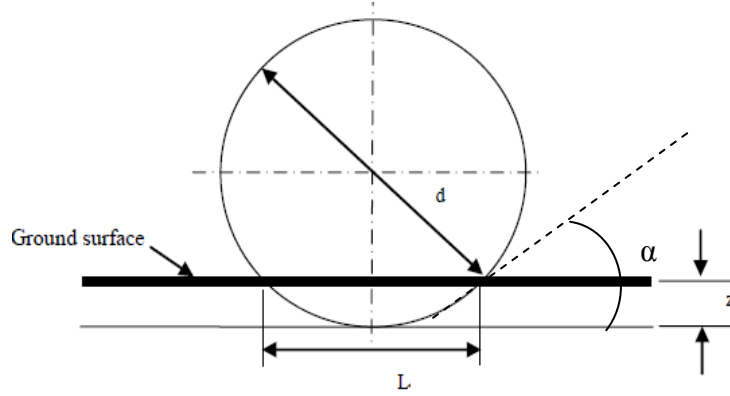
Fig. 2.5: Rigid wheel ground contact length (Radziszewski, et al., 2009)

shown by experimental results in Chapter 4, section 4.4, then the only factors that can affect the ideal thrust are wheel load and the numbers of wheels. Bekker`s general model for effective thrust (H) for both plastic soils at low velocity and low slippage is:

$$H = H_0(1 - e^{-iL/k}) \qquad (2.6)$$

i is the slippage, k is the shear deformation slip modulus, L is the wheel-soil contact length. Slip is defined as follow:

$$i = \frac{r\omega - V}{r\omega} \qquad (2.7)$$

The effective thrust is definitely lower than the ideal thrust due to the slippage of wheel on a given terrain.

Using the Mohr-Coulomb criteria for the maximum shear stress, the actual shear stress beneath a wheel or truck was also investigated by Wong and Reece following Bekker`s model (Wong & Reece, 1967):

17

$$\tau = \tau_{max}\left(1 - e^{-j/K}\right) \tag{2.8}$$

Where j is the shear deformation along the wheel-soil interface and K is the shear deformation modulus. The shear deformation j along the wheel-soil interface beneath a track has been investigated by Bekker based on the analysis of the slip velocity (Wong & Reece, 1967). Following the same approach Wong and Reece developed j on the soil-wheel interface, in terms of the angle θ, wheel radius (r) and wheel slip (i) (Wong & Reece, 1967):

$$j = r[(\theta_1 - \theta) - (1 - i)(sin\theta_1 - sin\theta)] \tag{2.9}$$

By substituting equations (2.3) and (2.9) into equation (2.8), Wong's model for the shear stress around the wheel-soil interface as a function of angle θ could be expressed by the following equation:

$$\tau(\theta) = (c + \sigma(\theta)tan\varphi)\left(1 - e^{-r/K[(\theta_1 - \theta)-(1-i)(sin\theta_1 - sin\theta)]}\right) \tag{2.10}$$

Based on Wong's model, the effective thrust, H, can then be evaluated by substituting equation (2.10) into the first term of equation (2.2). In Wong's model, the thrust is also affected by soil properties such as the cohesion and internal friction angle. However, the effective thrust developed by Wong is also a function of wheel contact angle (entry angle) with soil.

18

$$H = rb \left\{ \int_{\theta_2}^{\theta_1} \tau(\theta) cos\theta d\theta \right. \tag{2.11}$$

$$= \int_{\theta_2}^{\theta_1} (c + \sigma(\theta) tan\varphi)(1$$

$$\left. - e^{-r/K[(\theta_1-\theta)-(1-i)(sin\theta_1-sin\theta)]}) cos\theta d\theta \right\}$$

2.2.3 Terrain Characteristics: Normal Pressure Distribution

As explained in the previous sections, drawbar pull is the difference between the effective thrust, H, and the total motion resistances, R. In section 2.2.2, the evaluation of effective thrust has been shown using the two models: Bekker versus Wong. In Bekker model, the effective thrust was shown to be a function of wheel contact area, soil geotechnical properties, as well as wheel slip. Wong's model also considers those variables mentioned for Bekker's model plus wheel contact angle with soil. In this section, we will present the estimation of motion resistances based on soil normal pressure distribution using the same two models.

In Bekker's model, several forces are responsible for motion resistances. For a wheel in a straight line motion on horizontal plane, the most important forces are caused by wheel sinkage and bulldozing. The overall resistance is the summation of these forces:

$$R = R_b + R_c \tag{2.12}$$

19

Bulldozing resistance (R_b) is caused by the pushing of soil in front of a wheel by the motion of that wheel and compaction resistance (R_c) is caused by wheel sinkage. The bulldozing resistance is developed as follow:

$$R_b = \frac{b \sin(\alpha + \emptyset)}{2 \sin\alpha \cos\emptyset} \left(2zck_c + \gamma z^2 k_\gamma\right) \tag{2.13}$$

$$+ \left(\frac{\pi \gamma l_0^3 (90 - \emptyset)}{540} + \frac{\pi c l_0^2}{180} + c l_0^2 \tan\left(45 + \frac{\emptyset}{2}\right)\right)$$

where

k_γ: is the modulus of density of soil deformation

$$k_\gamma = \left(\frac{2N_\gamma}{\tan\emptyset} + 1\right) \cos\emptyset^2$$

α: is the angle shown in Fig. 2.5:

$$a = \cos^{-1}\left(1 - \left(\frac{2z}{d}\right)\right)$$

l_o: is the distance of rupture [m]

$$l_0 = z \tan\left(45 - \frac{\emptyset}{2}\right)^2$$

The other constants are provided in Table A1, APPENDIX A.

The soil used in the present study is dry sand with negligible cohesion, as shown by experimental results in Chapter 4, section 4.4. If ($c = 0$), therefore equation (2.13) reduces to the following form:

$$R_b = \frac{b\sin(\alpha + \emptyset)}{2\sin\alpha\cos\emptyset}(\gamma z^2 k_\gamma) + \left(\frac{\pi\gamma l_0^3(90 - \emptyset)}{540}\right)$$

where R_b mostly depends on wheel sinkage (z).

Sinkage is developed as a result of an applied load to the terrain through the running gear of a vehicle. The pressure-sinkage relationship for a homogeneous terrain, at a given depth, was characterized by Bekker's empirical equation (Wong J. , 2010) following "Bernstein (1913) and Goriatchkin (1937) empirical model" (McKyes, 1985):

$$p = (k_c/b + k_\emptyset)z^n \tag{2.14}$$

Where p is the pressure beneath the wheel applied by wheel load on the soil surface, b is the smallest dimension of the contact patch; that could be the width of a rectangular contact area or the radius of a circular contact area, z is sinkage, and n, k_c, and k_ϕ are pressure-sinkage parameters. The compaction resistance is computed by integrating the pressure equation (2.14) from ground contact to the maximum sinkage as follow:

$$R_c = b \int_0^z (k_c/b + k_\emptyset)z^n dz \tag{2.15}$$

$$R_c = \frac{(k_c + bk_\emptyset)z^{(n+1)}}{n + 1} \tag{2.16}$$

The values for n, k_c, and k_ϕ can be determined by conducting a minimum of two penetration tests with two sizes of plates having different widths (or radii). Multi-plate penetration testing performed by Fan (1985) proved that the accuracy

21

of k_c, k_ϕ, and n increases with increased number of test having different plate width or radius size. Therefore, an accurate result for soil stiffness moduli requires more than two tests. Furthermore, based on Bekker and Wong observations, in order to minimize the uncertainty in applying the measured data to the prediction of wheel performance, the size of the plate used in the tests should be comparable to that of the contact patch of a wheel. To this end, a device called Bevameter has been originally conceived by Bekker and built at the University of Newcastle upon Tyne and later extensively modified at Carleton University by Wong in order to measure the pressure-sinkage parameters (Wong J. , 2010). This device was also used and described in Taylor (2009). In this thesis, a Bevameter was not accessible; therefore the pressure-sinkage parameters have not been found experimentally, but taken from the literature for compact dry sand, see Table A1 in Appendix A.

In Wong's model the motion resistance is primary due to wheel sinkage. The pressure-sinkage equation (2.14) proposed by Bekker is based on the assumption that the normal pressure on the wheel circumference is related to the pressure beneath a sinkage plate at the same depth, assuming that the maximum normal pressure beneath a wheel is always located at the bottom-dead-center, for example at the lowest point of contact on the wheel rim in soil. However, in the method developed by Wong and Reece (1967) the location of maximum normal pressure beneath a wheel varies with slip; at higher slips (e.g. 100% slip) the location of the maximum normal pressure ,θ_m, moves towards the entry angle, θ_1, and the exit angle, θ_2, increases, see Fig. 2.6.

22
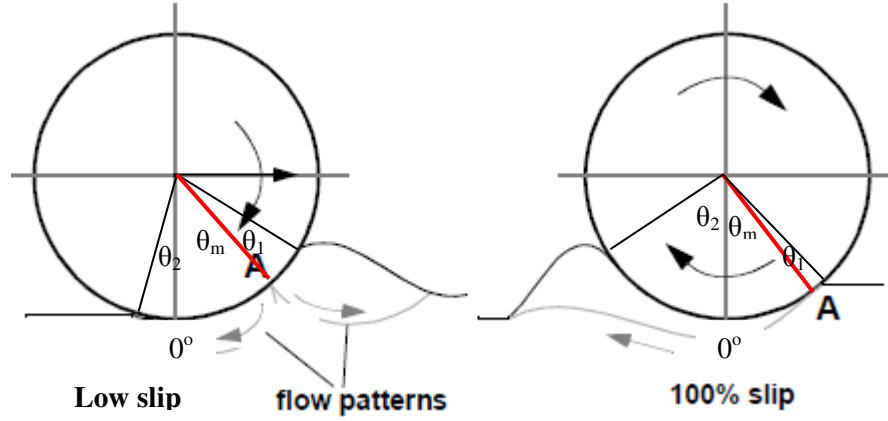
Fig. 2.6: Soil flow at soil-wheel interface during driving at low slip (left) and at 100% slip (right), (Apostolopoulos, 2001)

The point A in Fig. 2.6 identifies the maximum radial stress where the two soil failure zones beneath the wheel join each other. Theoretically, it is not possible to locate this point. However in Wong and Reece (1967) several sets of experiments have been done on different type of sands in order to determine a relationship between the locations of maximum point of stress (θ_m), the entry angle (θ_1) and slip (i). Fig. 2.7 shows the graph of one of the experiments done on dry sand. Based on the results, shown in Fig. 2.7, the location of θ_m could be expressed by equation (2.17), where the ratio of θ_m to θ_1 varies linearly as a function of slip, i. The coefficients c_1 and c_2 (see Appendix A) have been found experimentally by Wong and Reece (1967).

$$\frac{\theta_m}{\theta_1} = c_1 + c_2 i \qquad (2.17)$$
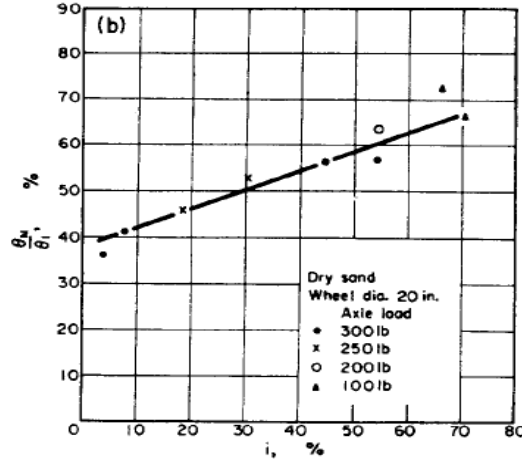
Fig. 2.7: Variation of the relative position of the maximum radial stress point with slip (Wong and Reece, 1967)

Following Wong's model, the radial stress from the beginning of contact θ_1 to the maximum radial stress point θ_m, called the "front region" (Fig. 2.6) is developed as follow:

$$\sigma_1 = (k_c + k_\phi b)(\frac{z}{b})^n \tag{2.18}$$

Where
$$z = (cos\theta - cos\theta_1)r \tag{2.19}$$

From the maximum radial pressure point θ_m to the end of contact θ_2 called the "rear region", the radial stress is calculated as follow:

$$\sigma_2(\theta) = (k_c + k_\phi b)(\frac{r}{b})^n \left[cos\left(\theta_1 - \left(\frac{\theta - \theta_2}{\theta_m - \theta_2}\right)(\theta_1 - \theta_m) \right) - cos\theta_1 \right]^n \tag{2.20}$$

Considering the two radial stress expressions, the total resistance to motion can be shown by the following equation:

$$R = \int_{\theta_m}^{\theta_1} \sigma_1(\theta)sin\theta d\theta + \int_{\theta_2}^{\theta_m} \sigma_2(\theta)sin\theta d\theta \qquad (2.21)$$

The effective thrust, equation (2.11), is also a function of radial stress σ (θ); the front and rear regions of equation (2.11) can be determined by equations (2.18) and (2.20).

Based on the equilibrium equation (2.2), the expression for drawbar pull is the algebraic summation of the x components of equation (2.21) and equation (2.11) (Wong and Reece, 1967):

$$DP = rb \left\{ \int_{\theta_m}^{\theta_1} \tau_1(\theta)cos\theta d\theta + \int_{\theta_2}^{\theta_m} \tau_2(\theta)cos\theta d\theta \right. \qquad (2.22)$$

$$\left. - \int_{\theta_m}^{\theta_1} \sigma_1(\theta)sin\theta d\theta - \int_{\theta_2}^{\theta_m} \sigma_2(\theta)sin\theta d\theta \right\}$$

The equilibrium equation for wheel motion in y direction as shown in Fig. 2.2 is developed following Wong and Reece (1967) model:

$$W = rb \left\{ \int_{\theta_2}^{\theta_1} \sigma(\theta)cos\theta d\theta + \int_{\theta_2}^{\theta_1} \tau(\theta)sin\theta d\theta \right\} \qquad (2.23)$$

By using equations (2.11), (2.18), and (2.20), equation (2.23) is expressed as follows:

$$W = rb \left\{ \int_{\theta_m}^{\theta_1} \sigma_1(\theta)cos\theta d\theta + \int_{\theta_2}^{\theta_m} \sigma_2(\theta)cos\theta d\theta \right. \qquad (2.24)$$

$$\left. + \int_{\theta_m}^{\theta_1} \tau_1(\theta)sin\theta d\theta + \int_{\theta_2}^{\theta_m} \tau_2(\theta)sin\theta d\theta \right\}$$

Where W is the total wheel load. The expression (2.24) is used to determine the entry angle θ_1 when W is known experimentally. The entry angle θ_1 is

subsequently used in equation (2.22) to determine the DP value. The MatLab code developed for determination of drawbar pull as a function of wheel total load, using Wong and Reece (1967) model, is attached in Appendix A.

As shown by Wong's drawbar pull model, in equation (2.22), several parameters affect the drawbar pull values. These variables are soil geotechnical properties, wheel geometry such as wheel radius and width, total wheel load and wheel entry and exit angles (θ_1, θ_2). θ_2 is an important parameter in the evaluation of drawbar pull when testing wheels at very high degree of slip. As shown in Fig. 2.6, θ_2 increases with slip. When there is a considerable amount of soil on the back of a wheel, the soil mass acts similar to a support for the wheel and creates a reaction force that adds up to the amount of force available for wheel to advance. In Chapter 4, section 4.5, the difference in drawbar pull values obtained by Wong's model for 2 different exit angles: 1- for 0° and 2- at high exit angles is shown.

2.3 Experimental Technique Background

There are two different techniques to measure the drawbar pull: the controlled-slip technique and controlled-pull technique. Fig. 2.8 shows a single wheel testbed setup that was used by Murphy and Green (1969) to measure the drawbar pull using the two techniques. In that setup, the wheel is attached to a carriage and connected by a load cell to a sled on which different loads (M_3) could be applied. In a controlled-slip test, the angular velocity of the wheel is kept constant, however slip is controlled by varying the velocity of the carriage (M_2, the mass of M_1 is negligible), the sled is not engaged. In a controlled-pull technique, the angular velocity of the wheel is also held constant, the carriage drive is not engaged, but external loads on the sled are applied. The application of various constant normal loads produces various amounts of slips. The net tractive effort was measured by carriage cell (F_6) in both techniques. More explanation about the mechanics of the system and the equations used to determine the net drawbar pull considering resistance and inertial force due to mass M_1 could be found in Murphy and Green (1969).
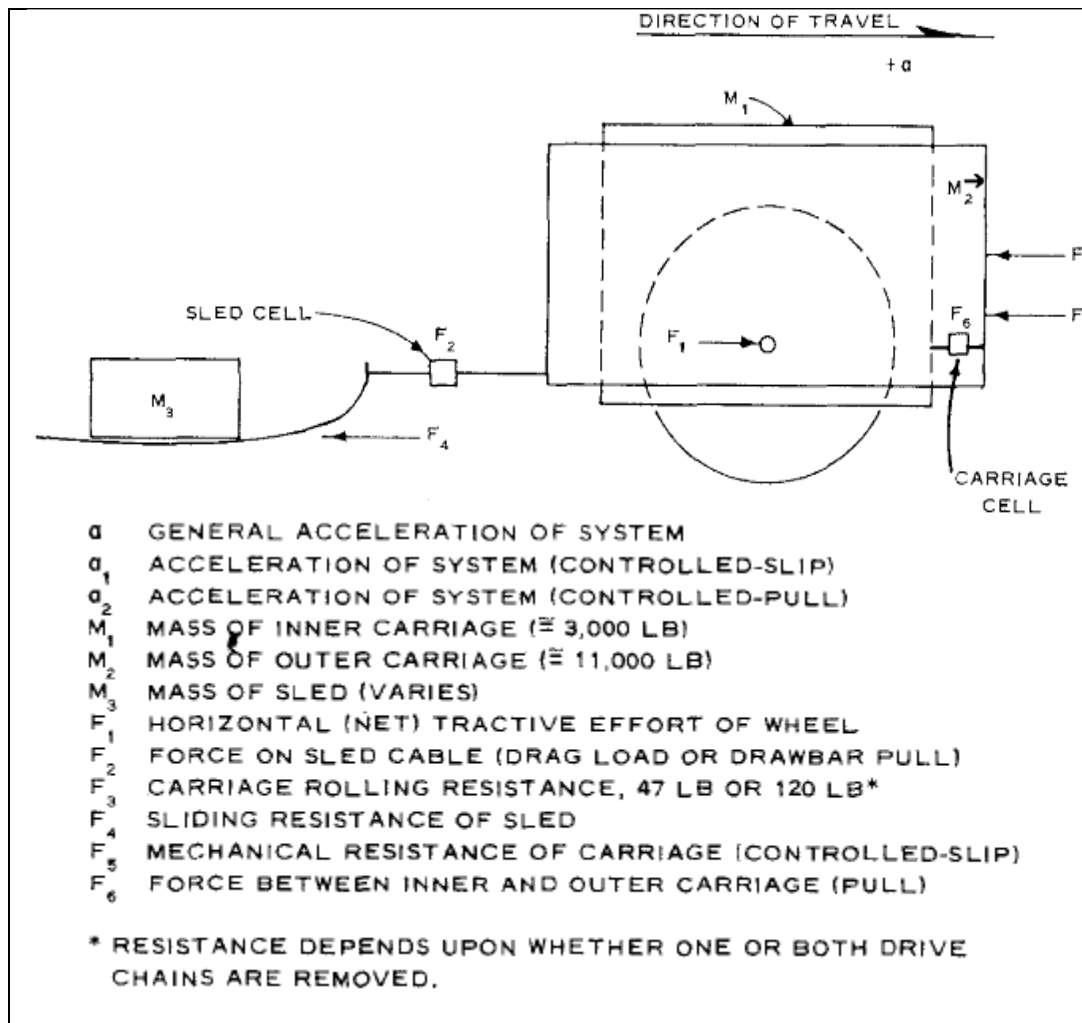
Fig. 2.8: Single wheel dynamometer system schematic (Murphy and Green, 1969)

Further single wheel testbeds with different configurations have been used by several researchers to investigate the wheel-soil interaction performance for planetary rovers as well as agricultural vehicles. The mobility performance criteria were evaluated in a controlled-slip manner in terms of overall motion resistance, drawbar pull, drive torque and energy consumption when operating under typical wheel loads on a range of specified soil. Results from single-wheel performance could be used to predict the overall locomotion performance. The use of single wheel tests was proved to be an acceptable practice in the design of

28

all-wheel drive locomotion (Apostolopoulos, 2001). As outlined in Apostolopoulos (2001), previous experimentation performed with various wheel types and scale models demonstrated that the difference between the drawbar pull performance of a wheeled rover rolling on sand and the predicted drawbar pull from single powered wheel tests in similar sand conditions is insignificant.

Fig. 2.9 presents some of the past and current single wheel testbeds followed by their respective references. Fig. 2.9 (a) shows a single wheel testbed used in the US Army Engineer Waterway Experiment Station (WES) in 1970 to test and determine the relative performance of different lunar prototype wheels under light loads for the Apollo mission program and to establish a better understanding of the basic principles of wheel-soil interactions (Freitag,et al., 1970).

Fig. 2.9 (b) illustrates a single wheel setup at DLR German Aerospace Center to test the mobility performance of flexible wheels intended for the ExoMars rover, a mission planned by the European Space Agency to land the rover on Mars by 2018 (Patel, et al., 2010).

Fig. 2.9 (c) is a single wheel testbed used at Carnegie Mellon University to quantify the in soil performance of a single robotic wheel with different grouser positions. The testbed also allowed for continuous wheel driving, endurance test, and negotiation of hard obstacles as those that could be found on the surface of Mars (Apostolopoulos, 2001).

The single wheel testbed of Fig. 2.9 (d) was developed at Cranfield University (Silsoe) for performing pneumatic wheel-soil interaction tests at heavy wheel loads for agricultural purposes. The testbed can be adjusted for any free rolling deformable or rigid wheel (Patel and Godwin, 2008).

Fig. 2.9 (e) illustrates the single wheel setup developed at the Massachusetts Institute of Technology. The project undertaken by Kang (2003) was to develop an on-line estimation method of two important soil parameters, cohesion and internal friction angle. The analytical model was based on Wong's non-linear rigid wheel-deformable terrain model that was simplified in a linear function and therefore could employ the onboard wheel performance parameters from the single wheel testbed experiments as its inputs and estimate the internal friction angle and soil cohesion of the soil (Kang, 2003).

Fig. 2.9 (f) demonstrated the terramechanics rig at Virginia Tech Advanced Vehicle Dynamics Lab. In Taylor (2009), the effect of wheel diameter and width size on tractive performance was experimentally analyzed through the use of the single wheel testbed. The results showed that the drawbar pull and driving torque and therefore energy are directly correlated with wheel contact length (wheel diameter) and wheel width. A wheel with a wider or larger contact patch will produce higher values of driving torque and drawbar pull than a wheel with smaller contact patch. Greater drawbar pull values required higher energy and torque values, therefore wheel design should consider the balance between energy consumption and drawbar pull requirements (Taylor, 2009).
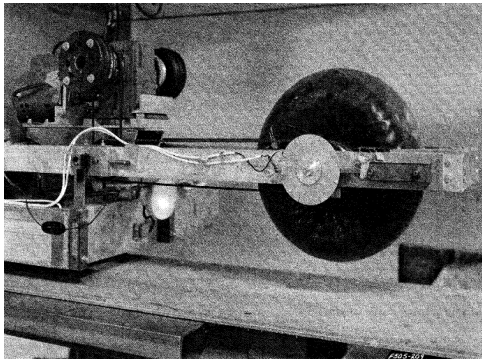
a) Lunar exploration (Freitag, et al.,1970)
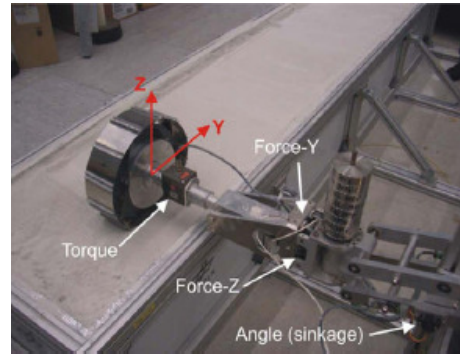
b) Mars exploration (Patel, et al., 2010)

c) Mars exploration (Apostolopoulos, 2001)

d) Agricultural studies (Patel and Godwin, 2008)
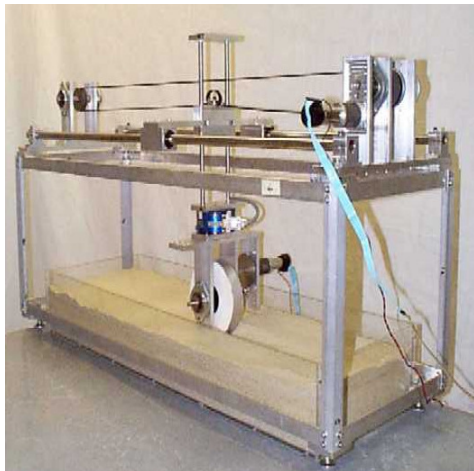
e) Mars exploration (Kang, 2003)

f) Lunar exploration (Taylor, 2009)

Fig. 2.9: Different single wheel testbeds for planetary and agricultural vehicle wheels investigation

Fig. 2.10 shows a typical experimental graph of drawbar pull versus slip performed by Murphy and Green (1969). From the graph of Fig. 2.10, it can be seen that the maximum drawbar pull is achieved at about 25% slip after which the pull starts to decrease. The expression for slip is described by equation (2.7). The trend of drawbar pull versus slip is always the same in all other experiments done by different researchers. The difference is in the values of drawbar pull achieved at various slips for different wheels and test conditions. Examples can be found in following references: Wong J. , 2010; Taylor, 2009; Wilkinson and DeGennaro, 2007; Patel, et al., 2004; Apostolopoulos, 2001; Freitag, et al., 1972; Wong & Reece, 1967.
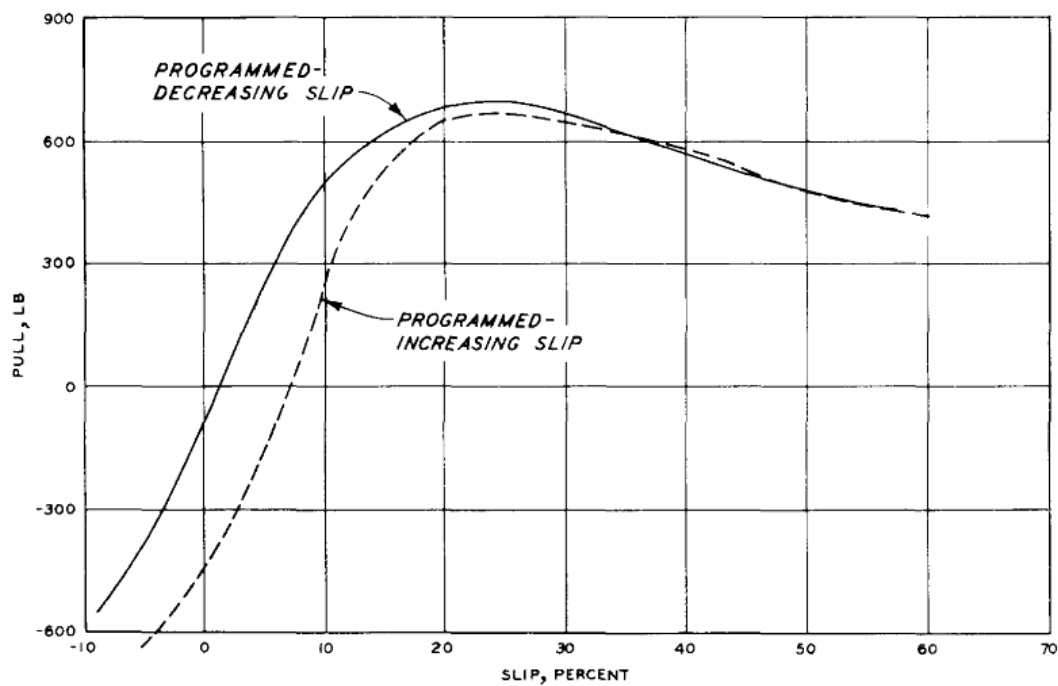
Fig. 2.10: The curves of drawbar pull as a function of slip (Murphy & Green, 1969)

In the present research, the test conditions did not allow for a precise measurement of slip, therefore wheels' drawbar pull was evaluated at 100% slip,

as a function of varying applied loads. Previous studies performed on single wheels by Taylor (2009) showed that the graphs of drawbar pull versus slip for various loads overlap at very low slip values, at about 5% slip (see Fig. 2.11 for an example). As seen from the figure, the graphs do not overlap after the 5% slip. Therefore, comparison of different wheels drawbar pull versus wheel total load at 100% slip is acceptable.
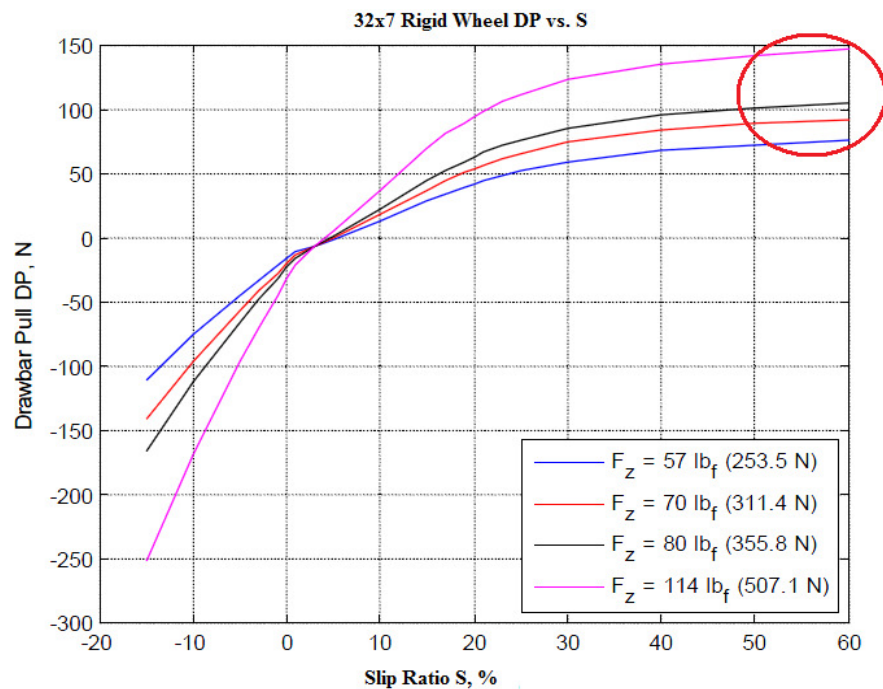
Fig. 2.11: Drawbar pull vs. slip for different normal loads (Taylor, 2009)

Evaluation of wheel's drawbar pull versus total wheel load for a given wheel slip (more than 5%) has already been investigated. Fig. 2.12 (Freitag, et al., 1972) and Fig. 2.13 (Freitag, et al., 1970) show the curves of drawbar pull versus varying loads respectively for heavily loaded and lightly loaded wheels at 20% slip. As shown in Fig. 2.12, the developed pull increases with increasing weight on the wheel up to a certain value after which the trend is reversed. The maximum drawbar

pull is therefore achieved at an optimum wheel weight (Sharma and Pandey, 2001).

In Fig. 2.13, the curve is ascending and the loads were not sufficient for both wheels

to achieve the maximum drawbar pull.
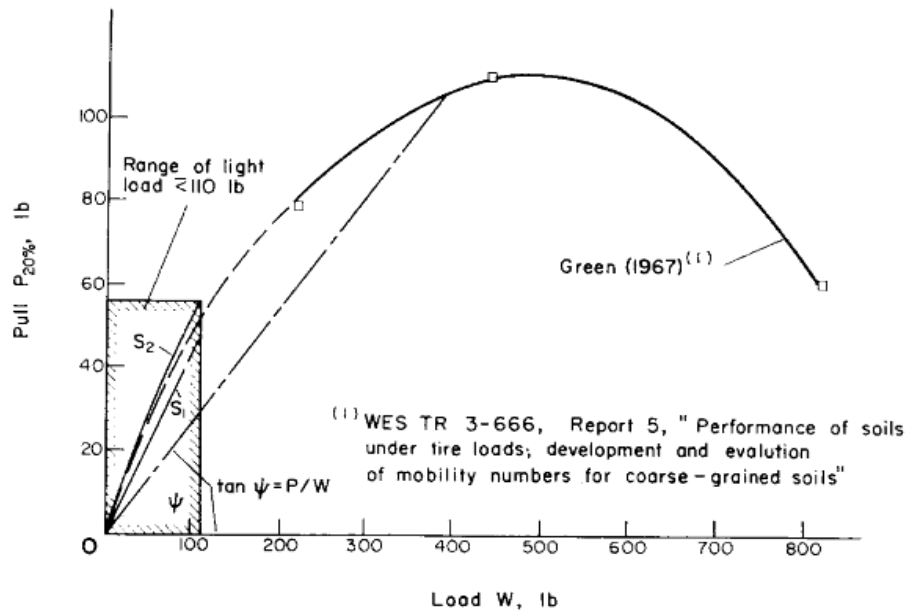
Fig. 2.12: Relation of drawbar pull to load of a pneumatic wheel for loaded wheel on dense, air-dry Yuma sand (Freitag, et al., 1972)
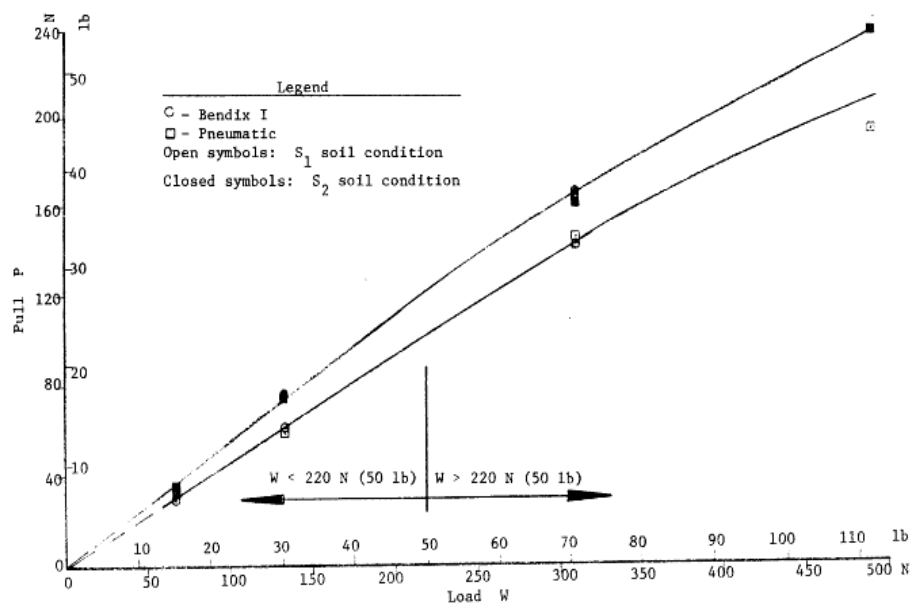
Fig. 2.13: Relation of drawbar pull to load for lightly loaded wheels (Freitag, et al., 1970)

34

The graph of drawbar pull versus total load also provides information about the maximum angle that a vehicle can climb given the same terrain conditions (Freitag, et al., 1972). The maximum climbing angle is obtained from the inverse tangent of the slope of drawbar pull to load at low loads; where the curve is almost linear. Experiments by Freitag, et al. (1972) demonstrated that the maximum angle actually climbed by a vehicle was approximately 3 degrees less than the inverse tangent of the slope obtained from the graph of drawbar pull to load of a single wheel, tested on a horizontal plane, on similar sand conditions. Initially, the 3 degrees difference in climbing angle was meant to be accounted for in the results for this research; however, by realizing that the test conditions and soil types are different, therefore the 3 degree difference in angle could not be applicable for our experiment. Further testing with a wheeled rover on different inclined terrains and similar sand conditions need to be investigated in order to experimentally evaluate the difference between the angles obtained from a horizontal plane.

2.4 Summary

This chapter provides an overview of theoretical analysis of rigid wheel-deformable terrain interaction based on Wong's and Bekker's models. More specifically it explains the semi-empirical equations to determine wheel drawbar pull when rolling on sand by considering the developed thrust and motion resistances. In general, Bekker's model supposes that the normal pressure acting on the wheel with a given width is equal to normal pressure acting on a flat plate of the same width at the same depth. However, experimental results from Wong

have shown that in practice, the maximum normal pressure distribution does not occur at the lowest contact point of the wheel, but rather at the intersection of the soil flows beneath the wheel which is a function of wheel slippage.

This chapter also explained the experimental techniques background by showing previous testbeds used by different researchers and experimental results that are generally observed for wheel performance characterization.

Chapter 3

Experimental Setup and Methodology

This chapter provides a description of the prototype wheels and explains the experimental apparatus, and the testing procedures for evaluation of their performance. The last section provides the experimental method in determining soil geotechnical properties and soil preparation technique.

The prototype wheels were grouped in three different diameter sizes: 5", 8", and 22". A single wheel testbed and two reduced controllable rovers were used to measure their performance. The performance measurements were evaluated in terms of:

a) the drawbar pull at 100% wheel slip with varying normal loads

b) hill climbing ability

c) the power consumption and coefficient of rolling resistance at low speed and negligible slip conditions

3.1 Description of Prototype Wheels
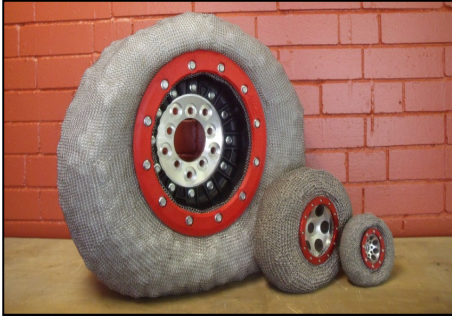
Five different prototype wheels with a diameter of 22" (55.9 cm) were used. Table 3.1 identifies and illustrates the wheels. Additionally, the wheel weights (W) and widths (b) are given. To examine the effect of wheel size on the tractive performance, the iRing wheel (Table 3. 1d) and the benchmark Rubber wheel (Table 3. 1e), at low pressure, were reproduced at two smaller sizes: 8" (20.3 cm) and 5" (12.7 cm) diameters, as shown in Table 3.2.

Wheel 1 (Chu, et al., 2009) and Wheel 2 (Gabrielli, et al., 2009) were made by undergraduate teams for their final projects and meant to be elastic metal wheels, however the metal used in their fabrication was very thick and therefore their degree of deflection was less than 10% of the wheel diameter, thus these wheels were considered as rigid wheels. Metal Wheel 1 (Table 3. 1a) has a smooth surface to which 10 small V-shaped grousers are attached to provide more traction in both wheel directions. The Metal Wheel 2 (Table 3. 1b) is the heaviest wheel and it has a smaller deflection than Wheel 1. Its surface is made of 16 metal plates that are hinged together. Each plate has 10 holes that are equally spaced from each other, initially made to reduce the overall wheel weight. The Brush Wheel (Table 3. 1c) was made out of surface cleaning brushes. The white hub is made out of a rigid plastic material, therefore, it does not deform, but the brush wheel surface can deflect on its length (2.5 cm). The iRing wheel (Table 3. 1d) is the only prototype wheel that can deform plastically. It is not elastic and does not bounce at all when dropped from a height. The iRing wheel's surface is made of a flexible chainmail

fabric and it is filled with particulates. One of the ideas behind this concept is to provide a wheel that can be filled with resources on the Moon surface, In Situ Resource Utilization (ISRU). For this experiment, the 22" diameter iRing wheel is filled with delrin balls, 1" diameter polypropylene solid balls, with a bulk density of 0.8s.g. The smaller scale iRing wheels are filled with dried peas. The iRing wheel concept is based on energy dissipation as opposed to storing it and releases the energy in an elastically compliant structure (Radziszewski, et al., 2010). A more detailed description of the concept of iRing wheel can be found in Radziszewski et al. (2010). The bench mark Rubber wheel is a commercial wheel used for off-road rovers. The Rubber wheel at 7 psi is a rigid wheel, but the Rubber at 2.5 psi deflects at least 10% of the wheel diameter when loads of 40 N and more are applied.

a) Wheel 1 W = 289.1 N b = 25.5 cm	b) Wheel 2 W = 378.1 N b = 20.5 cm	c) Brush wheel W = 267 N b = 22.5 cm
d) iRing wheel W = 169 N b = 18.1 cm	e)Rubber wheel Pressure = 2.5psi W = 106.8 N b = 24.5 cm	f) Rubber wheel Pressure = 7 psi W = 106.8 N b = 24.5 cm

Table 3. 1: 22" diameter prototype wheels

iRings		Rubbers	
b_8"= 8 cm	W_8"=20.9N	b_8"=5.4 cm	W_8"=8.0N
b_5" = 4 cm	W_5"=2.9 N	b_5" = 9.5 cm	W_5"=1.5 N

Table 3. 2 : 3 scales of iRing and Rubber wheels
(Diameters from left to right: 22", 8", 5")

3.2 Experimental Setup

3.2.1 Drawbar Pull Test: 22" Diameter Wheels

All the tests for drawbar pull (DP) were measured at 100% wheel slip with varying the normal loads on the wheel. Traction tests for the 22" diameter wheels were conducted by using a single wheel testbed (Dennerlein, et al, 2009) (see Fig. 3.1b). The testbed consists of a metal structure, capable of supporting the wheel and axle assembly across a test surface. Presently, the testbed only allows for a straight line motion of the wheel. The test surface is made of a 3 m x 1.5 m x 0.25 m sandbox, filled with dry sand. The wheel vertical motion is made possible through sliders that can move up to 0.5 m. A camera support is attached to the carriage system, on the opposite side of the wheel, and its location is presented by the white letter "C" in the testbed image of Fig. 3.1b. Each wheel drawbar pull test at various loads was recorded in order to observe the contact angles made by the wheel soil interaction at 100% slip for use in Wong model.

40

The weight on the wheel can be controlled through a counterweight system that is connected by pulleys on the opposite side of the wheel carriage and fixed to a slider that gives the possibility to move along the testbed length following the wheel motion (see Fig. 3.1a). In order to add weight on the wheel, one needs to remove weights from the weight stack. The relationship between the weight on the weight stack and the actual weight beneath the wheel was measured as shown in Fig. 3.2. From the linear fit of Fig. 3.2, the total weight beneath the wheel can be found using the equation (3.1).

a) counterweight system   b) single wheel testbed
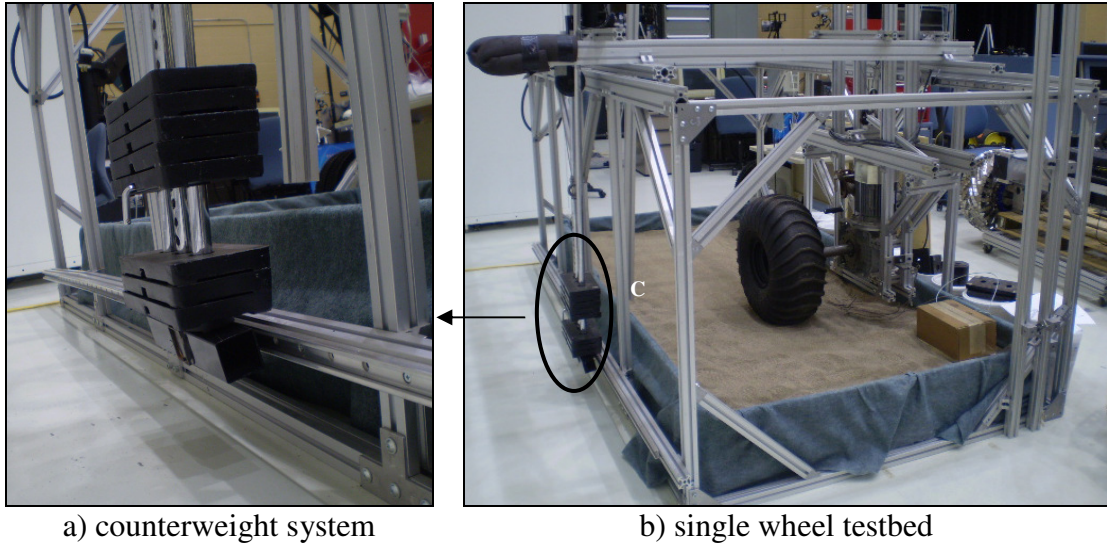
Fig. 3.1: Single wheel testbed structure and counterweight system

$$y = -3.897x + 1094.1 + F_w \qquad (3.1)$$
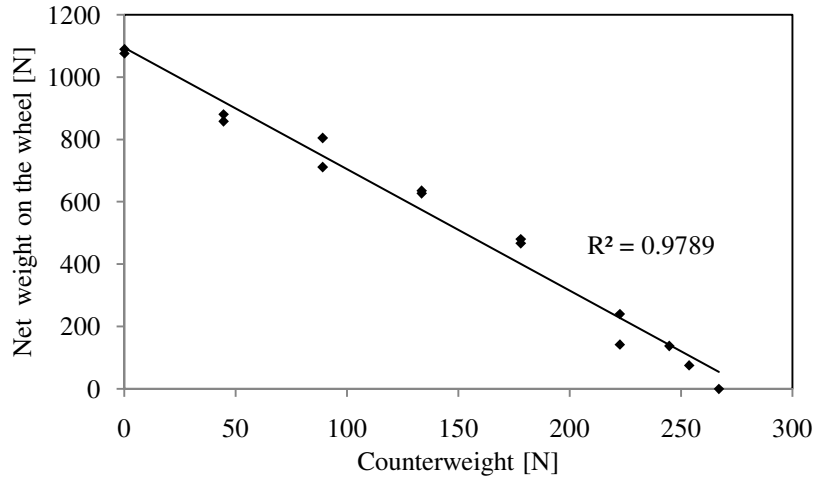
Fig. 3.2: Single wheel testbed counterweight calibration

where

F_w wheel weight [N]

x weight on the counterweight [N]

y total weight beneath the wheel [N]

According to Fig. 3.2, the maximum load that can be applied beneath a wheel is about 1100 N plus the wheel weight.

The drawbar pull measurements were performed using a load cell. The load cell was attached to the wheel carriage by a pre-stretched cord, in line with the wheel centre, and was fixed, on the other end, to the testbed frame by a metal rod. Fig. 3.3a) shows the setup and Fig. 3.3b) demonstrates the stretched cord during the maximum pull test on the wheel.
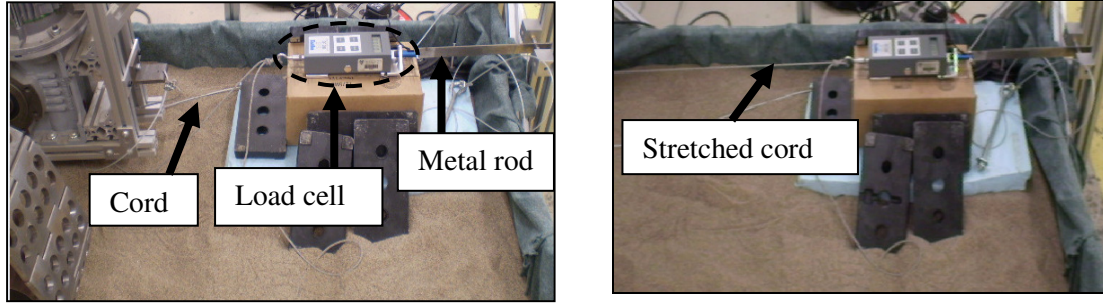
a) Before test   b) At 100% wheel slip

Fig. 3.3: Load cell setup on the single wheel testbed

The tension in the cord was read at 100% wheel slip, at varying wheel loads and with a motor angular velocity of 0.44 rad/s. The actual DP force was determined by considering the added force due to sliders friction on the single wheel testbed, as shown by equation 3.2. The friction force, $F_{friction}$, was

$$DP_{actual} = DP_{load\ cell} + F_{friction} \qquad (3.2)$$

determined by measuring the pulling force of the wheel carriage system horizontally with the load cell with the prototype wheel lifted off the soil surface, prior to each test. The load cell was attached to the frame and positioned in line with the wheel center. The process was repeated several times for each wheel and the average value was added for each DP load cell readings.

3.2.2 Drawbar Pull Test: 5" and 8" Diameter Wheels

The 5" and 8" diameter wheels were tested on two reduced scale controllable rovers (Radziszewski, et al., 2010) (see Fig. 3. 4a, b). The drawbar pull test was performed by using a load cell, following the same procedure as for the 22" diameter wheels. Fig. 3. **5** demonstrates the load cell setup for the 8"

43

diameter wheels; this setup was also used for the 5" diameter wheels. The loads were added to each rover by fixing them on top of the rover, in such a way as to obtain an equivalent load for each wheel.

a) Testbed for 5"diameter wheels   b) Testbed for 8" diameter wheels

Fig. 3. 4: Testbed platforms for 5" and 8" diameter wheels
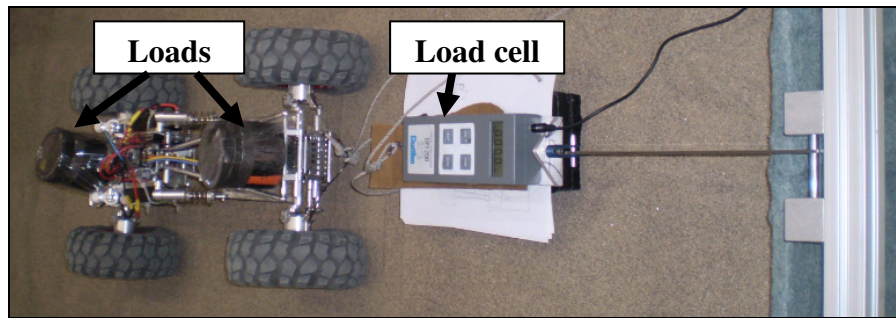
Fig. 3. 5: Load cell setup for 5" and 8"diameter wheels

3.3 Power Consumption Test

3.3.1 Power Consumption: 22" Diameter Wheels

A 3-phase AC induction motor and a gear box with a gear ratio of 46:1 were used to drive the 22" diameter wheels in the testbed (see Fig. 3.6). A

Variable Frequency Drive controller (VFD-S, Model: VFD022S21U) was connected in between the power supply and the motor. The VFD system was used to control the rotational speed of the AC electric motor by controlling the frequency (f) of the electrical power supplied to the motor. The frequency could be changed via the VFD software interface that was connected by a USB key from the controller to the computer. The current (I) and voltage (V) fed to the motor could be tracked every 0.5 second time step from the VFD software interface. Fig. 3.7 shows the single wheel testbed power diagram, the VFD position, and the setup for the load cell and the camera which can move horizontally to keep track of the wheel motion.

Fig. 3.6: Single wheel testbed: motor and gear box assembly
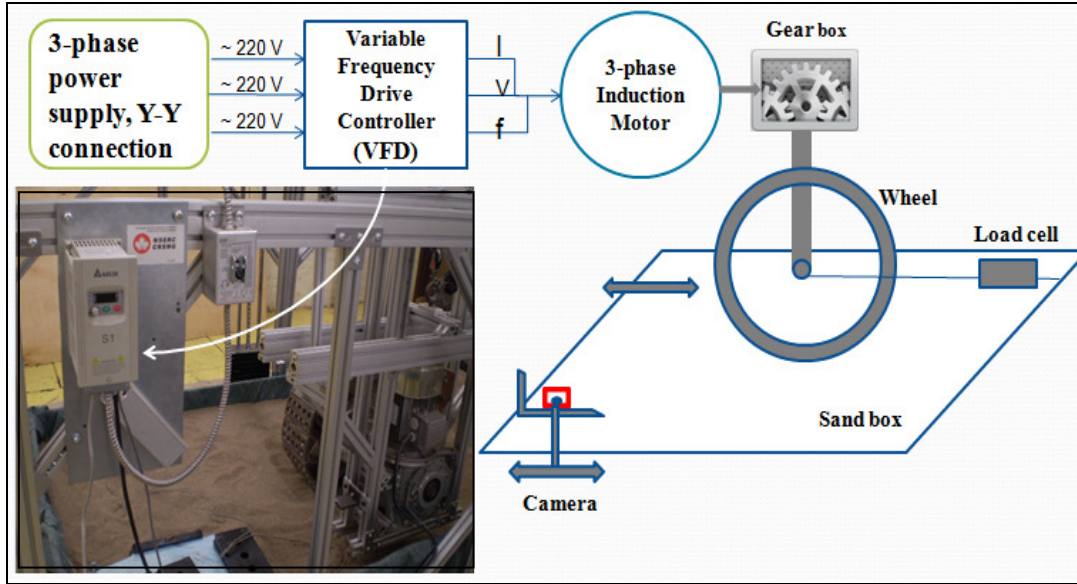
Fig. 3.7: Single wheel testbed power diagram

The 22" diameter wheels power consumption was performed over 1 meter distance in the soil bin area, at different normal loads and varying speeds. The wheel linear speed was measured by keeping track of the time over the distance X (1 m), as shown in Fig. 3.8. The linear speeds varied between 0.04 to 0.15 m/s at negligible slip. The power consumed by the 22" wheels from the 3-phase induction motor (Y-Y connection) was calculated from the equation (3.3) (McPherson, 1981):

$$P = P_{in} - P_{loss} \qquad (3.3)$$

$$P_{in} = \sqrt{3}\,(V.I).\cos(\theta) \qquad (3.4)$$

P_{in} is the power input to the motor

$\cos(\theta)$ is the motor power factor (0.77).
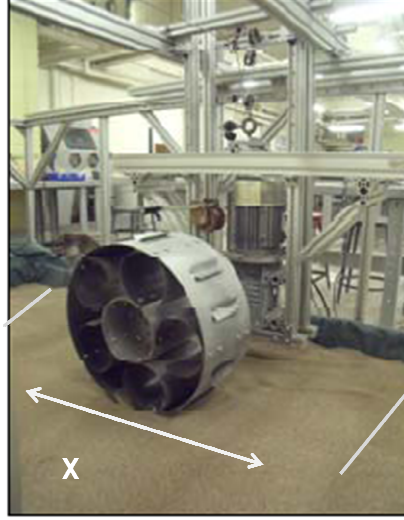
Fig. 3.8: Power consumption test, 22" diameter wheels

P_{loss} is the power loss due to carriage friction and wheel inertia [W] and is explained below.

$$P_{loss} = \left(F_{friction}.v\right) + P_{inertia} \tag{3.5}$$

v is the wheel linear velocity [m/s].

The voltage (V) and current (I) values used in equation (3.4) were taken from the VFD controller. The graph of current versus time step (see Fig. 3.9) shows an example of data generation from the VFD controller for the 22" rubber wheel at two different loads. The current values used in equation (3.4) were averaged from the steady state conditions, delimited by the two black lings on each graph in Fig. 3.9. Using the same time step intervals, the voltage values were also averaged. The value for the friction force, $F_{friction}$ in equation (3.5), was taken from the $F_{friction}$ in equation (3.2).

47
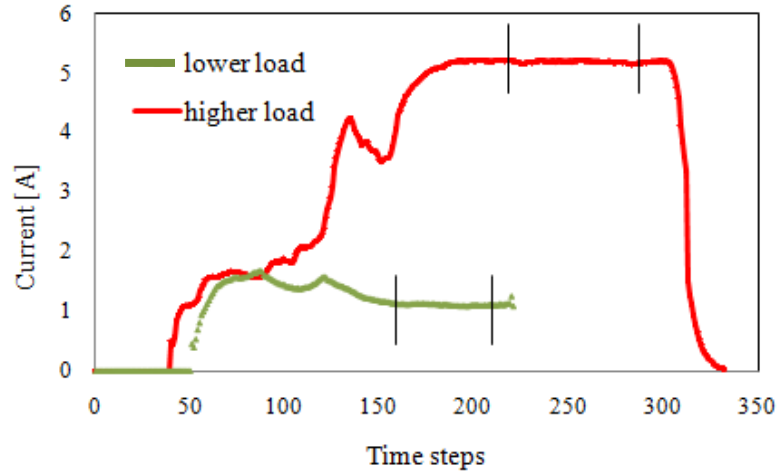
Fig. 3.9: Current vs. time step for Rubber wheel at 2 different wheel loads

The power loss due to inertia, $P_{inertia}$, and other source of losses in equation (3.5) was obtained after running the experiments and plotting the graphs of power versus velocity. More precisely, the initial value of power at zero velocity for each wheel and load condition was considered as the overall loss and subsequently subtracted from each data point, ensuring that at zero speed, the power is zero. An example is shown by the graph of Fig. 3. 10, where the initial value of power, 23.4 W is obtained from curve fitting.

$$y = 764.14x + 23.383$$
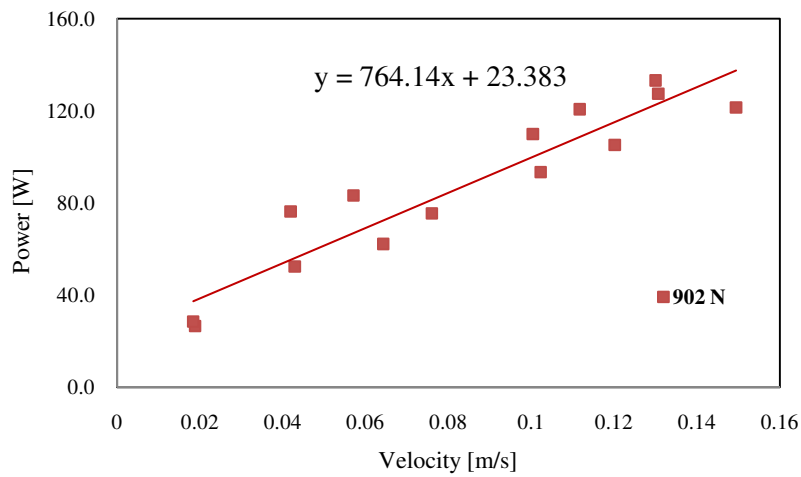
Fig. 3. 10: Example of power vs velocity graph

3.3.2 Power Consumption: 5" Diameter Wheels

The power consumption test for the 5" diameter iRing and rubber wheels was completed at low velocities ranging from 0.05 to 0.4 m/s, at negligible slip, and at varying normal loads. The power consumption test for the 8"diameter wheels could not be performed due to technical problems with the 8" wheel rover testbed.

Fig. 3.11 illustrates the overall apparatus for the 5" wheel power consumption test. The rover used a brushless DC motor. The current and voltage used by the small scale controllable rover could be read simultaneously from a multimeter device. The multimeter was connected via two long electrical wires from the rover battery to the motor. More precisely, one wire was attached in series with the current branch and the other was connected in parallel to the voltage branch of the motor-battery connection region. A camera was held fixed to record simultaneously the current and voltage from the multimeter screen and to trace the travel time up to $1/1000^{th}$ of second precision from the start to the end point of the traveled distance. Each test for the 5" wheel was repeated at least 3 times over a distance of 1 meter during which the rover had reached the constant velocity conditions.

For a brushless DC motor, the power is calculated by the product of the voltage and current. Once again, the power consumed was calculated following equation (3.3). However, for the rover, each term of the equation (3.3) was expressed simply by equations (3.6) and (3.7). The power loss due to inertia

($P_{inertia}$), in equation (3.7) was found using the same approach as explained by Fig. 3. 10.

$$P_{in} = V.I \qquad (3.6)$$

$$P_{losses} = P_{inertia} \qquad (3.7)$$
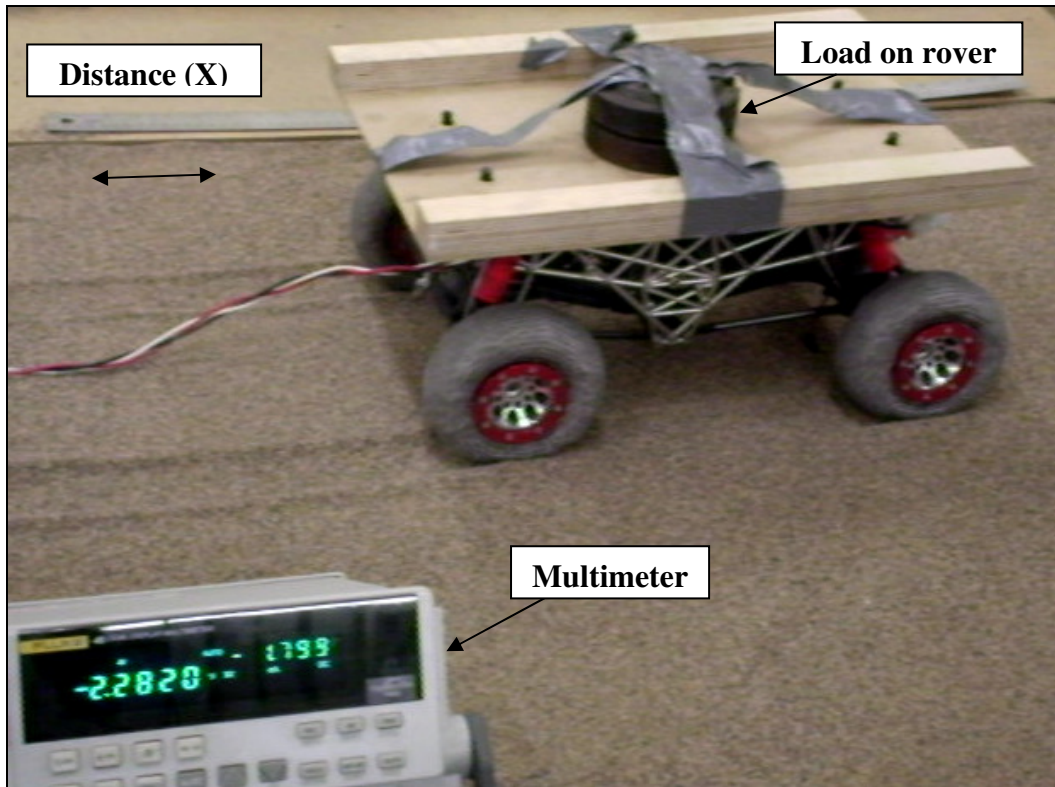
Fig. 3.11: Power consumption test (5"wheels)

3.3.3 Coefficient of Rolling Resistance

The coefficient of rolling resistance for each wheel, for a given load, was evaluated from the power consumption test based on the equation (3.8) (Radziszewski, et al., 2009):

$$C_r = {}^P\!/_{(W.v)} \qquad\qquad (3.8)$$

where

C_r Coefficient of rolling resistance [1]

P Power consumed by the wheel [W]

W Total weight on the wheel [N]

v Wheel linear velocity [m/s]

3.4 Soil Geotechnical Properties Measurement

Two important soil parameters, the internal friction angle and cohesion, were experimentally found using a direct shear box. Soil parameters were used in Bekker and Wong's semi-empirical equations to compare the experimental drawbar pull as a function of total wheel load.

A direct shear test machine (see Fig. 3.12) is made of the following major parts: a direct shear box as illustrated in Fig. 3.13, a proving ring that is in contact with the upper part of the direct shear box in order to measure the horizontal force applied to the specimen, and a yoke by which the normal load can be applied to the soil specimen. The horizontal load is applied by a motor and gear box arrangement to the lower part of the shear box, from the left side of the machine. To measure the shear strength of the dry sand, a constant mass of the specified dry sand was filled in the shear box, layer by layer in order to provide a uniform

51

distribution of soil surface in the box. The shear box was placed in the direct shear machine area, as shown in Fig. 3.12 and a chosen load was placed on the area for load application purposes. The motor was run at very low speed, 1mm/s, and graph of soil shear stress as a function of soil deformation was retrieved from the computer. This experiment was repeated for five other normal loads and each test was repeated at least three times.
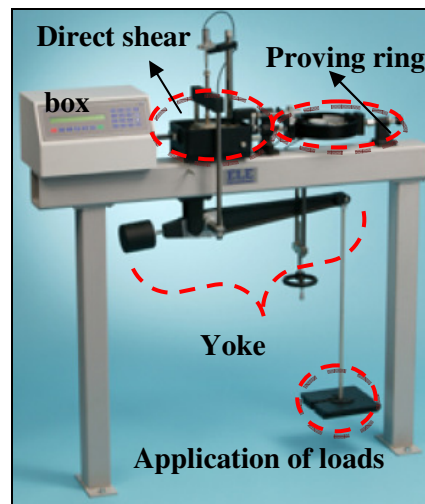
Fig. 3.12: Direct shear test machine
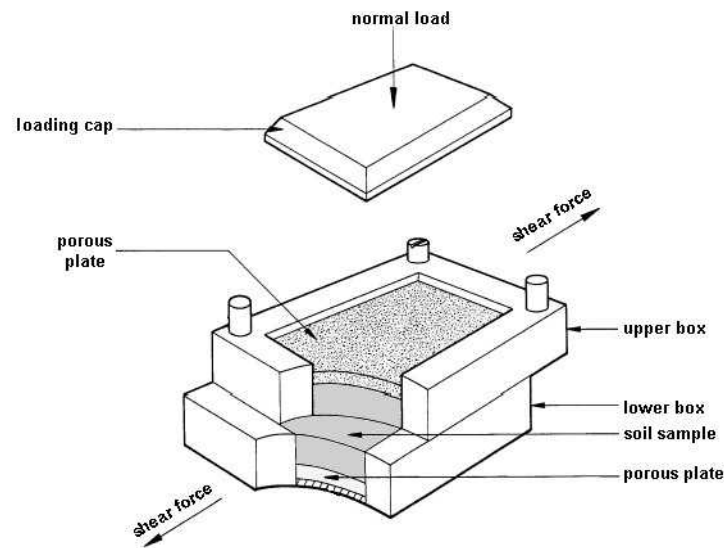
Fig. 3.13: Direct shear box (geotechnical shear strength of soil by direct shear test)

Fig. 3.14 shows a typical graph of shear stress versus horizontal deformation of two different types of soils at a given normal stress. In the type A soil, the shear stress tends towards a constant value or asymptote. This behavior is usually observed in consolidated clay and in loosely accumulated sandy soils. However, in the type B soil, the shear stress reaches a maximum value before decreasing to a minimum value, which is called the residual force. This trend is observed in overconsolidated clays and in compacted sandy soils (Muro and O'Brien, 2004). Soil cohesion and internal friction angle can be determined from the graphs of Fig. 3. 14 using Coulomb`s failure criterion (equation 2.3). By repeating the test for different normal loads, and then recording the peak shear stress for each normal load, a graph of shear stress versus normal stress can be made, as shown in Fig. 3. 15. For type A soil, since there is not a maximum value, therefore the maximum shear stress value is that measured at a horizontal displacement of about 8 mm or 50% of the initial thickness of the soil sample (Muro and O'Brien, 2004).
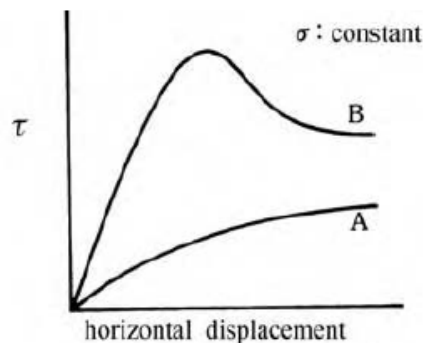
Fig. 3. 14: Relationship between shear strength and horizontal displacement for two types of soil (Muro and O'Brien, 2004)

53
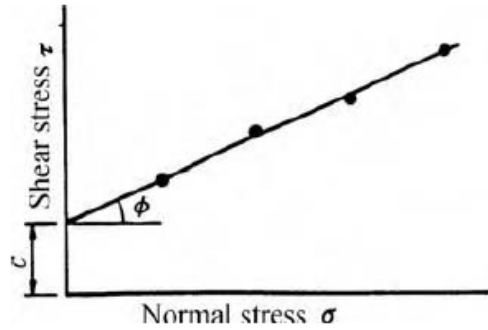
Fig. 3. 15: Determination of soil cohesion (c) and internal friction angle (φ)
(Muro and O'Brien, 2004)

3.5 Soil Preparation Technique

In this section a brief description of the soil preparation method prior to each wheel traction test for the 5", 8", and 22" diameter wheels is explained. A more detailed technique of soil preparation for single wheel tests has been investigated by (Taylor, 2009). In this research experiment, prior to each test, the soil surface was well mixed with a shovel and then levelled with a 15"x5"x2" flat piece of wood and a leveller. The levelled soil surface was compacted by applying a 10lb force on the wood surface as shown in Fig. 3. 16. This method was repeated along the 1 meter distance for the wheel travel.

Fig. 3. 16: Preparation of the soil surface prior to wheel testing

3.6 Summary

This chapter provides the detailed description of the prototype wheels and the experimental setup to measure their traction performance. The traction performance was measured in terms of the wheel drawbar pull and power consumption. A single wheel testbed apparatus was used for the 22`` diameter wheels and two small scale rovers were used for the 5" and 8" diameter wheels. A load cell was used for all wheel sizes to measure the drawbar pull force. For the 22" diameter wheels, the power consumption of the induction motor was recorded using a variable frequency drive controller, whereas the power consumed by the DC motor of the 5" diameter wheels rover was measured through a multimeter.

Soil geotechnical properties such as the internal friction angle and cohesion were measured by using a direct shear box machine. Soil preparation technique prior to each wheel testing was briefly explained.

Chapter 4

Results and Analysis

This chapter presents the experimental results for the traction performance of the 5", 8", and 22" diameter wheels. The traction performance was measured in terms of drawbar pull as a function of total wheel load, the slope climbing ability for each wheel, wheel power consumption versus velocity and total wheel load, and the coefficient of rolling resistance. Section 4.4 provides data on soil geotechnical properties and the values obtained for soil cohesion and internal friction angle. In section 4.5, Bekker and Wong's rigid wheel-deformable terrain interaction models are used to compare with the experimental drawbar pull results for three sizes of wheel diameters, 5", 8", and 22".

This chapter also analyses, compares and discusses the values obtained from the different wheel performance metrics and soil geotechnical properties.

4.1 Drawbar Pull Results

4.1.1 Drawbar Pull 5" and 8" Diameter Wheels

All the tests for the drawbar pull (DP) were measured at 100% wheel slip. Also, all DP values were normalized to wheel width, with the units in N/m. The DP graphs are presented for one wheel. Finally, to better compare the overall range of drawbar pull, the integrated average, DP$_{average}$, was used:

$$DP_{avg} = \frac{1}{L_{max} - L_{min}} \int_{L_{min}}^{L_{max}} DP \ dL \qquad (4.1)$$

where L_{min} and L_{max} are the load measurement limits for each particular wheel, and DP is the drawbar pull, which is a function of the load conditions , L.

Fig. 4. **1** shows the experimental data for the average normalized drawbar pull as a function of total wheel load. The green curve corresponds to the 5" and 8" diameter iRing wheels data points and the pink curve presents the 5" and 8" Rubber wheels results. The error bars on the experimental data represent the standard deviation of the drawbar pull values obtained from a number of tests performed for each load condition, where each test was repeated at least four times. The trend of the curves in Fig. 4.1 matches with the trend of the curves of drawbar pull versus load for lightly loaded wheels of Fig. 2.13, in litterature review, Chapter 2. The results from Fig. 4.1 shows that iRing wheels attain slightly higher drawbar pull values between 0 to 43N weight range. The integrated average DP, for both Rubber and iRing wheels of 5" and 8" diameters, was calculated over each wheels respective weight domains, delimited by the

black dashed line – each wheel had a DP determined for a given range of loads. The minimum load applied to the 8" wheels was greater than the maximum load applied to the 5" wheels. The results are tabulated in Table 4.1.
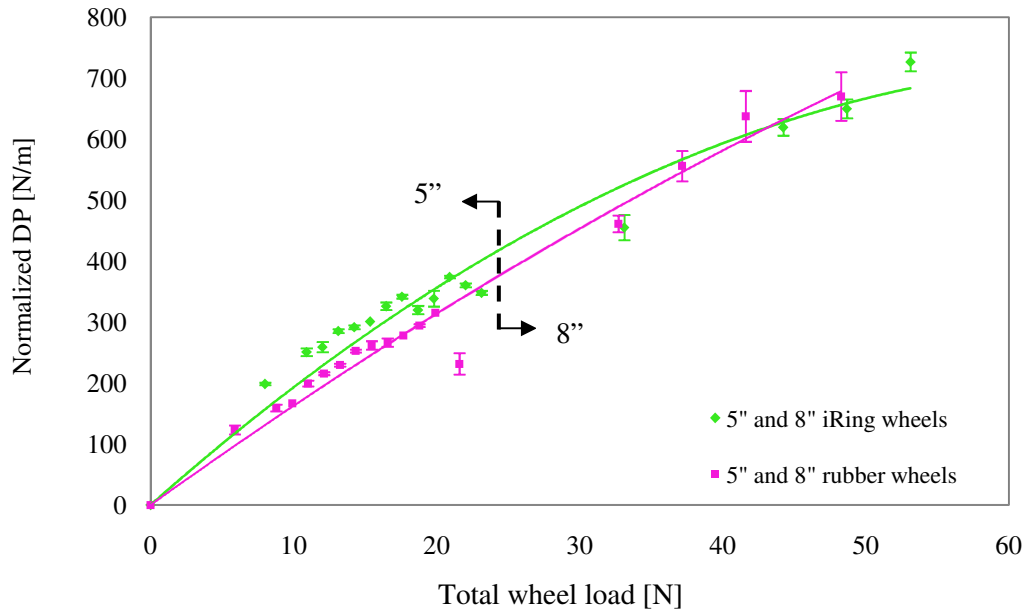
Fig. 4. 1: Normalized drawbar pull per wheel vs. Total wheel weight
(5" and 8" diameter iRing and rubber wheels)

The curves of Fig. 4.1 present parabolic fits of the measurements; from this, the optimum load at which the maximum drawbar pull can be achieved was calculated for each wheel type and is presented in Table 4.1. Rubber wheels can achieve higher drawbar pull values at higher weight capacity than iRing wheels. Finally, the climbing angles for both wheel types and sizes were calculated for each experimental point of the graph of Fig. 4.1.

Table 4.1: Comparison of 5" and 8" diameters iRing and Rubber wheels

Wheel Type_Size [in]	DP$_{avg}$ [N/m]	Optimum Weight [N]	Max. DP [N/m]	Avg. Climbing Angle [deg]
iRing_5	230.7			
iRing_8	365.2	69.7	759.9	28.1
Rubber_5	173.1			
Rubber_8	323.9	146.0	1265.5	32.1
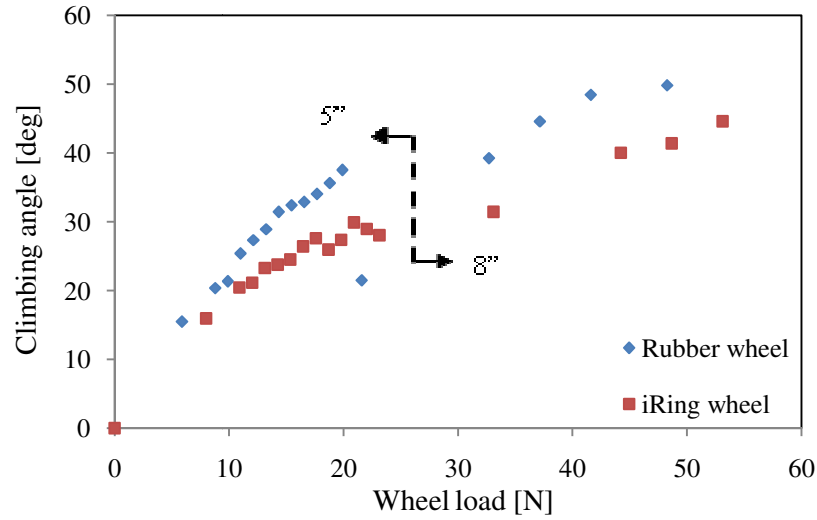
Fig. 4.2: Rubber vs iRing climbing angles as a function of wheel load

The results are presented in Fig. 4.2. As seen from this graph, the climbing angle increases with wheel load. Furthermore, rubber wheel achieves a slightly higher climbing angle than the iRing wheel, for both wheel diameter sizes, at 100% slip. The average climbing angle is therefore higher for rubber wheel, as given in Fig. 4.2.

4.1.2 Drawbar Pull 22" Diameter Wheels

Fig. 4.3 shows the experimental drawbar pull results for three 22" diameter wheels: iRing wheel, Rubber at 7 psi, and Rubber at 2.5 psi. The small portion of the graph at lower loads, contoured with the dotted box, shows the previous results from 5" and 8" wheels, better highlighting their trend with respect to the 22" diameter wheel equivalents. From the figure, the 8" diameter wheel results have higher slopes than the 22" wheels, which explain the difference in hill climbing ability when comparing the 8" rubber and iRing results in Fig. 4.2 to the climbing angle values of the 22" Rubber at 2.5 psi and iRing wheels in Table 4.2, computed at a load of 200N. The climbing angle values for the 8" wheels are higher than for the 22" wheels.
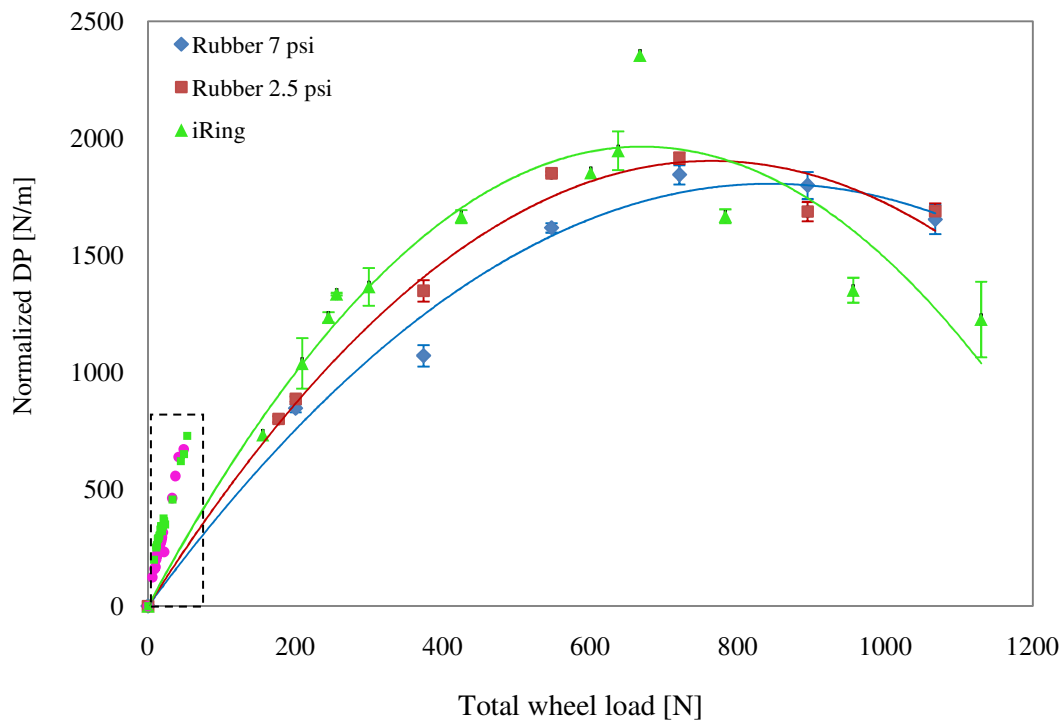
Fig. 4.3: Normalized drawbar pull per wheel vs. Total wheel load
(5", 8", and 22" iRing and rubber wheels)
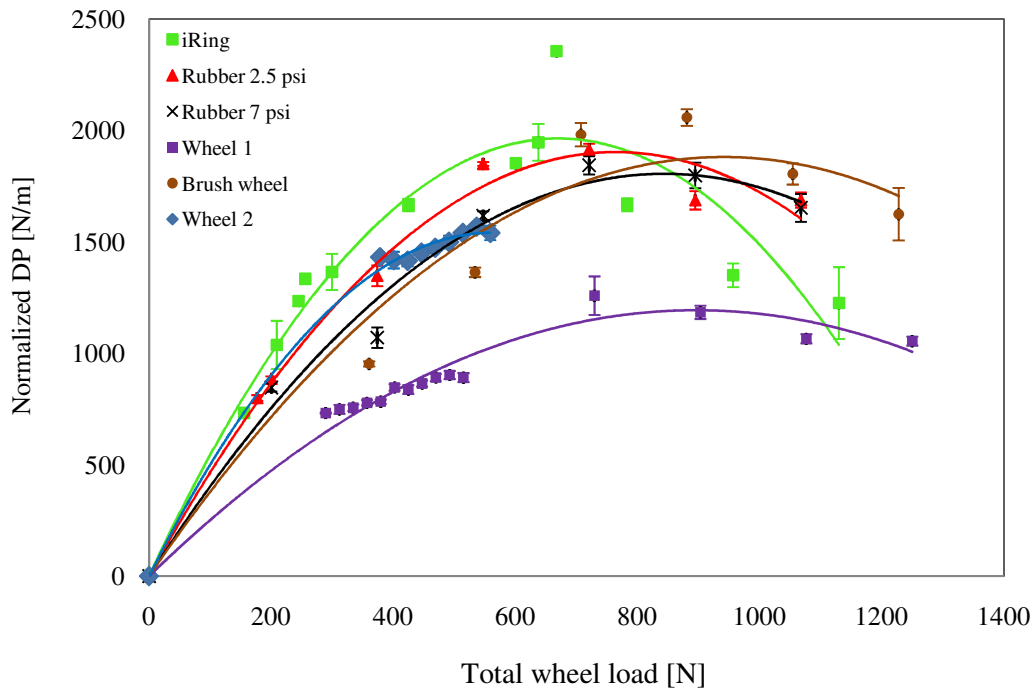
Fig. 4.4: Normalized drawbar pull per wheel vs. Total wheel weight
(22" diameter wheels)

Fig. 4.4 shows the experimental normalized drawbar pull graphs for all the

22" diameter wheels with a motor angular velocity of 0.44rad/s. The error bars on

the experimental data, in Fig. 4.3 and Fig. 4.4, represent the standard deviation of

the drawbar pull values obtained from a number of tests performed for each load

condition, where each test was repeated at least three times. The trend of the

curves in Fig. 4.4 matches with the trend of the curves of drawbar pull versus load

for heavily loaded wheels of Fig. 2.12, in the litterature, in Chapter 2. From the

graphs of Fig. 4.4, it can be seen that the green iRing wheel curve can achieve the

highest normalized drawbar pull values up to approximately 800 N loads.

However, the curves of Rubber at 2.5 psi (the red curve), Rubber at 7 psi (the blue

curve), Brush wheel (the brown curve), and a part of Wheel 2 (the black curve),

also show comparative normalized drawbar pull values to that of the iRing wheel,

in the linear range, within a 10% error. On the other hand, Wheel 1 shows the lowest normalized drawbar pull values.

The integrated average under each curve of Fig. 4.4 was calculated up to a weight of 550 N, which is slightly below the optimum weight for Wheel 2 (refer to Table 4.2, third column). The results, presented in Table 4.2, show that the iRing wheel has the highest integrated average drawbar pull (DP_{avg}). From the same table, it can be observed, that the integrated average drawbar pull values for

Table 4.2: Comparison of 22" diameter wheels

Wheel Type_Pressure [psi]	DP_{avg} [N/m]	Max. DP [N/m]	Optimum Weight [N]	Climbing Angle at 200 N [deg]
iRing	1194	1921.0	662.8	32.8
Rubber_2.5	1026.1	1892.8	765.6	39.1
Wheel 2	963.3	1545.9	561.2	33
Rubber_7	884.7	1851.5	860	36
Brush	697.8	1913.8	934.8	34.3
Wheel 1	565.9	1242.1	928.6	24.5

Rubber at 2.5 psi, Wheel 2, and Rubber at 7 psi are very close to that of the iRing wheel result. Similarly, the iRing wheel achieves the highest maximum DP value (DP_{max}), as shown in Table 4.2. The maximum DP values for Rubber at 2.5 psi, Rubber at 7 psi, and Brush wheel are also about the same as that attained by the iRing wheel. It is interesting to note that the increase in drawbar pull for the iRing wheel and its closeness to the drawbar pull performance of the commercial Rubber wheel was achieved regardless of the presence of any grousers in its design. As it was described earlier, the iRing wheel surface was made out of a

chainmail fabric. Based on the idea that sand can get into the small pores and create sand to sand interactions, an increase in the thrust and the net drawbar pull is unsurprising. Conversely, Wheel 1 has the lowest DP_{avg} and DP_{max} values, since it had a smooth metallic surface and a small number of grousers compared to the size of the wheel. In Wilkinson and DeGennaro, (2007), the importance of number of grousers and their spacing is mentioned. In that paper, the number of grousers interacting with the soil has been investigated with the change in wheel diameter, given a fixed grouser spacing. It is mentioned that the soil shear stregnth decreases if the grousers are tall enough or close enough to disrupt the soil of neighboring grousers.

The Rubber wheel at 2.5 psi had an average drawbar pull higher than that of the Rubber wheel at 7 psi. The difference in drawbar pull between the two Rubber wheels is explained by the change in wheel contact patch; at lower pressure the wheel contact patch increases and therefore generates a greater net drawbar pull.

Lastly, Wheel 2 has an averaged drawbar pull higher than Rubber at 7 psi. The presence of holes on the surface of Wheel 2 and the sand to sand interactions explain this rise in drawbar pull. However, Wheel 2 was the heaviest wheel (see Table 3.1); therefore it does not present a practical comparison point in this experiment, as this wheel design is unpractical for any lunar mission.

In terms of the optimum weight and maximum drawbar pull, the iRing wheel has a higher maximum drawbar pull than the rest of the 22" wheels, but it

64

cannot support too much weight, its optimum weight or load is the second lowest, after Wheel 2, as seen in Table 4.2. The Brush wheel has the highest value in optimum weight and it can develop almost the same amount of maximum drawbar pull as the iRing wheel, see Table 4.2. The Brush wheel has a rigid hub, which explains its capability in supporting much higher loads, and the flexible brushes on the surface provide a high traction on sand. In the same manner, the Rubber wheel at 7 psi could withstand higher loads than Rubber at 2.5 psi, because of its rigidity due to the high pressure. However, the maximum drawbar pull for Rubber at 2.5 psi is a higher due to the increase in contact patch. The maximum climbing angle for each wheel was also calculated in the range of 0 to 100N total wheel weight. Based on the values given in Table 4.2, the Rubber wheel at 2.5 psi has the higher maximum climbing angle than the other wheels, and Wheel 1 has the smallest value.

4.2 Power Consumption

4.2.1 Power Consumption: 5" Diameter Wheels

Fig. 4.5 and Fig. 4.6 illustrate respectively the results of the average power consumption for a 5" diameter iRing wheel and a 5" diameter rubber wheel, as a function of velocity, at different normal loads, with their standard deviation error bars which were obtained from a number of tests performed for each load conditions; each test was repeated at least three times. As seen from both graphs, the average power increases linearly with increasing velocity and applied normal loads. The power consumed by iRing wheel is higher than that consumed by the

rubber wheel. The maximum average power consumed by the 5" iRing wheel is about 5 W at a velocity of 0.4 m/s for a 11.75 N load, whereas the power consumed by the 5" rubber at 0.4 m/s under a 11 N load is less than 2.5 W.
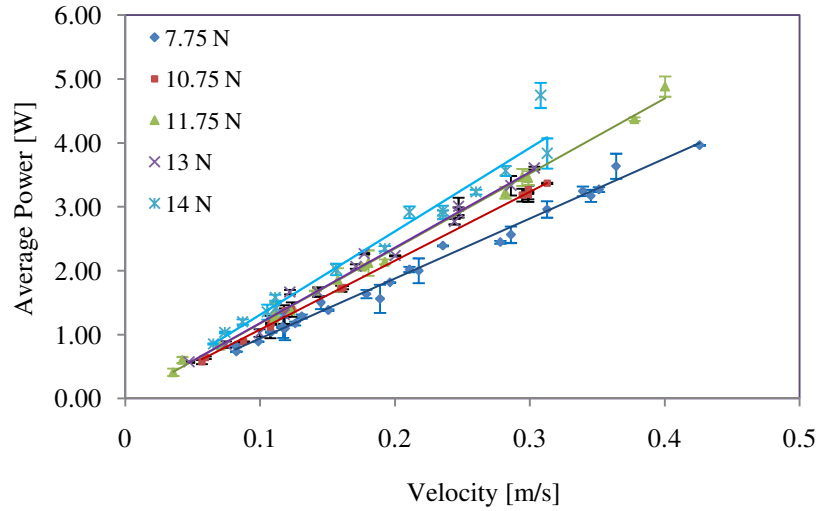
Fig. 4.5: Power consumption for one 5" iRing wheel versus velocity at different normal loads
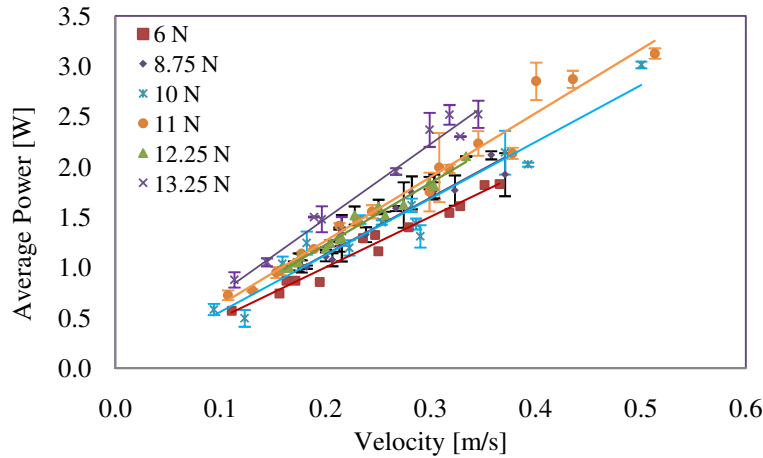
Fig. 4.6: Power consumption for one 5" rubber wheel versus velocity at different normal loads

From the linear equations of the graphs of Fig. 4.5 and Fig. 4.6, the power consumption at 0.3 m/s was calculated for every load, for both wheel types. The results are presented in the graphs of average power versus total wheel load in

Fig. 4.7. From the graph of Fig. 4.7, it is clear that power consumption increases linearly with total weight for both iRing and rubber wheel. Moreover, the graph shows that the 5" iRing wheel consumes about 2.5 times more power than the 5" rubber wheel at 0.3 m/s.
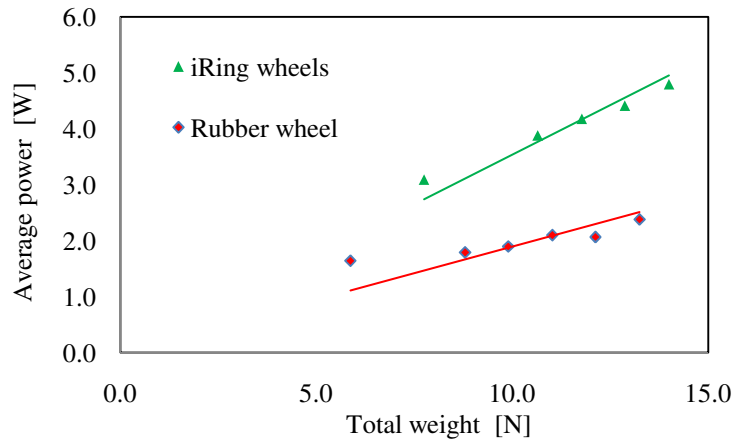
Fig. 4.7: Average power vs. total weight at 0.3 m/s (5" diameter iRing and Rubber wheels)

4.2.2 Power Consumption: 22" Diameter Wheels

Fig. 4.8 presents the results of average power consumption versus velocity for the 22" diameter wheels at various total wheel loads. Here, all the experimental data points are presented in each graph. It can be seen, from all six graphs that power consumption increases with increasing velocity and with increasing total wheel weight, as was the case for the 5" diameter wheels. The power consumption for each wheel type was calculated at 0.3 m/s wheel speed and the results are presented in Fig. 4.9, the graph of average power versus total wheel load. The 22" iRing wheel's power consumption is almost twice the 22" Rubber at 2.5 psi. The 22" iRing wheel has also the highest power consumption

curve similar to the 5" diameter iRing wheel's power consumption. In Fig. 4.9, iRing consumes about 7 times more power than the Rubber wheel at 7 psi. As it was expected by the iRing wheel concept, it dissipates energy as opposed to storing it. The Brush wheel consumes almost the same amount of power than the Rubber at 2.5 psi at the low load range, however the power consumption for Wheel 1's increases faster than the brush wheel's curve. Wheel 1 and Wheel 2 have the next highest power consumption curves, after the iRing wheel curve.

a) Wheel 1

b) Wheel 2

c) Brush wheel

d) Rubber_7 psi
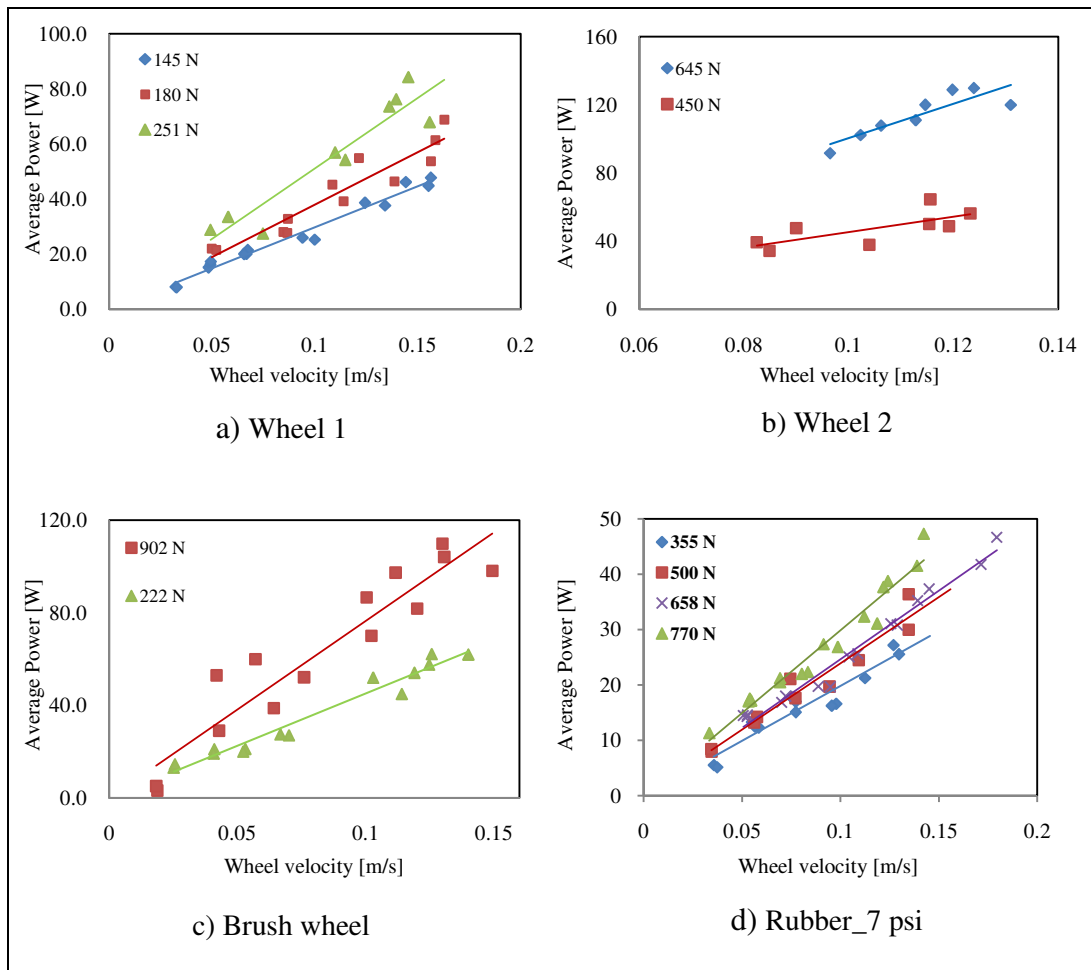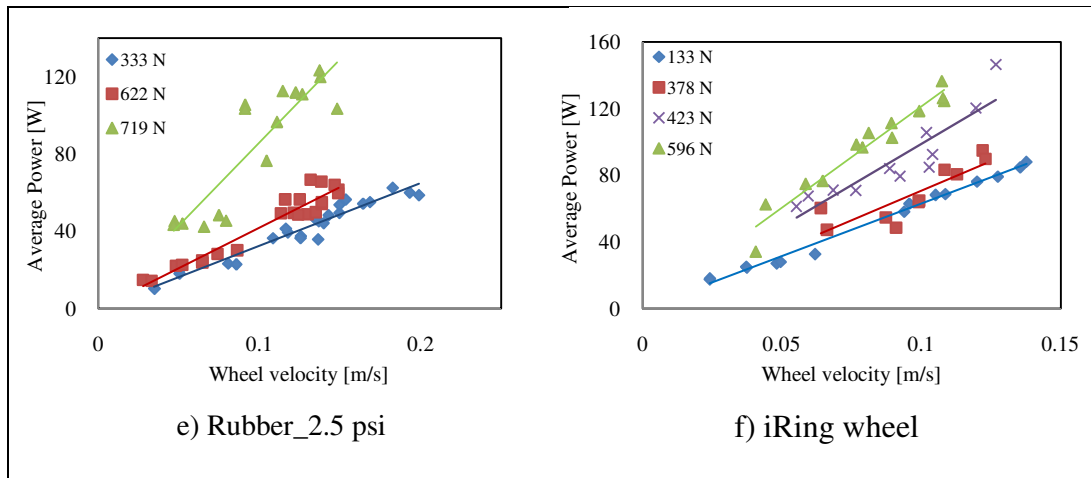
Fig. 4.8: Graphs of average power [W] versus wheel velocity [m/s] for 22" diameter wheels at different total wheel loads
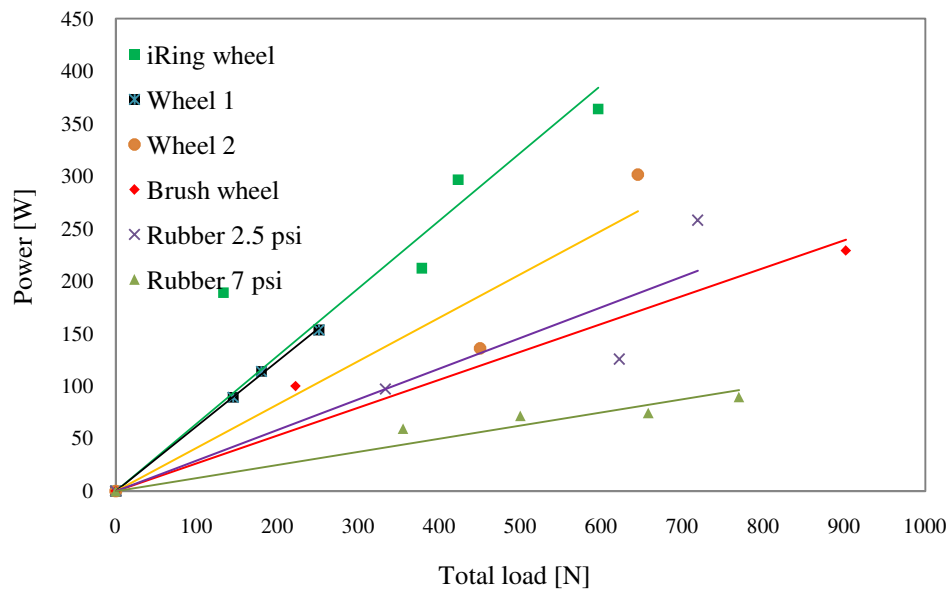
Fig. 4.9: Average power consumption versus total wheel load for 22" wheels at a velocity of 0.3 m/s

4.3 Coefficient of Rolling Resistance (Cr)

The coefficient of rolling resistance (Cr) is presented in Table 4.3 for the 5" wheels and in Table 4.4 for the 22" wheels. According to Table 4.3, the Cr value for the 5" iRing wheel is greater than that observed for the Rubber wheel.

The coefficient of rolling resistances for the 22" diameter wheels, see Table 4.4, are sorted in an ascending order. Rubber at 7 psi has the lowest value and iRing wheel has the highest value of Cr. As mentioned previously by equation (3.8), the Cr value is directly proportional to the amount of power consumed by each wheel, and since iRing wheel consumes the highest amount of power therefore it has the highest C_r (see Fig. 4.9).

Table 4.3: 5" diameter wheels Cr

Wheel	C_r
Rubber	0.62
iRing	1.01

Table 4.4: 22" diameter wheels Cr

Wheel	C_r
Rubber_7	0.46
Wheel 1	0.59
Rubber_2.5	0.97
Wheel 2	1.33
Brush	1.44
iRing	2.58

4.4 Soil Geotechnical Results

In this section, experimental results for two important soil geotechnical properties such as the internal friction angle and soil cohesion are presented. Fig. 4.10 shows the results of variation of shear stress on dry sand as a function of deformation using the direct shear test at varying normal stress. As seen from the graphs, the shear stress increases with deformation up to a certain value, and the curves of shear stress reach greater values at higher normal stresses. In Fig. 4.10, for small normal stresses, ranging from 21.5 kPa to 50 kPa, the shear deformation curves increases rapidly to a maximum value from which the rate of increase decreases very fast and the stress values tend to decrease very slowly. In the same figure, for normal stress tests at 50kPa and higher, the rate of increase for shear stress values are greater up to a certain value, but the decrease in shear stress is more pronounced than for those tested at lighter normal stresses, reaching a minimum stress value that is called the residual.

By taking the peak values of each of the shear stress curves from Fig. 4.10, the shear stress versus normal stress can be obtained, as shown in Fig. 4.11. From this figure, the values for soil cohesion and internal friction angle are obtained. Soil cohesion corresponds to the initial value of shear stress and the internal friction angle is the inverse tangent of the slope. From the graph, soil cohesion is 0, and the internal friction angle is 43.5 degrees.
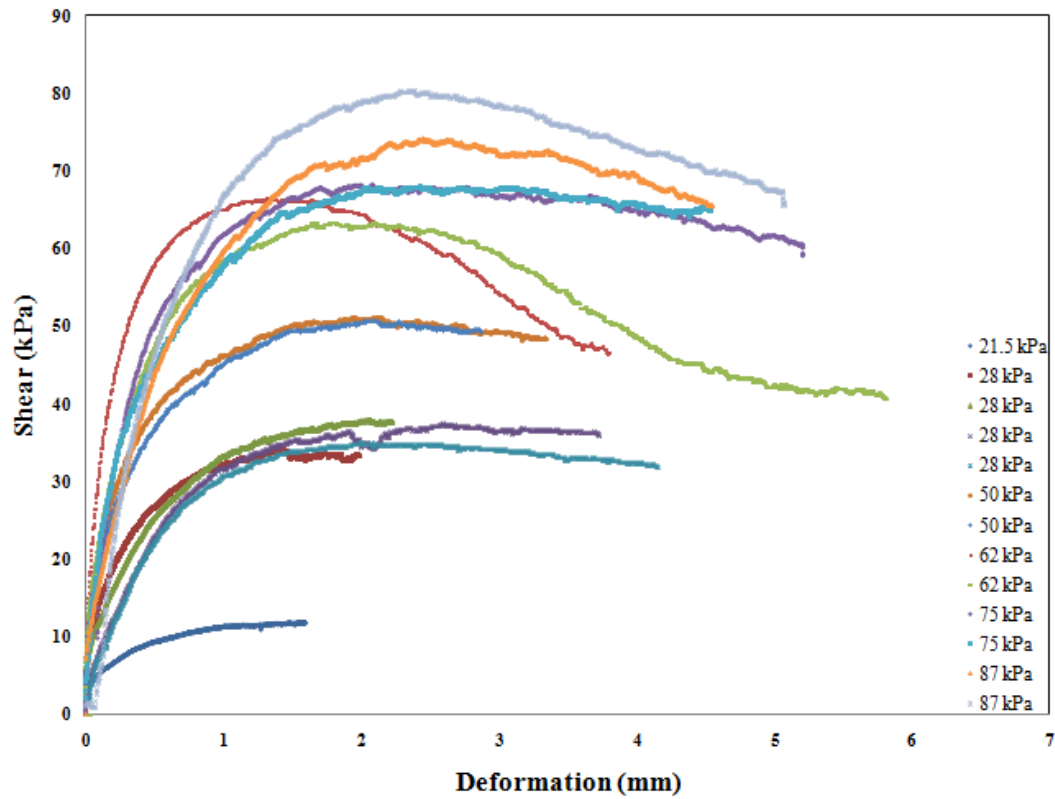
Fig. 4.10: Dry sand shear stress as a function of deformation with increasing normal stress
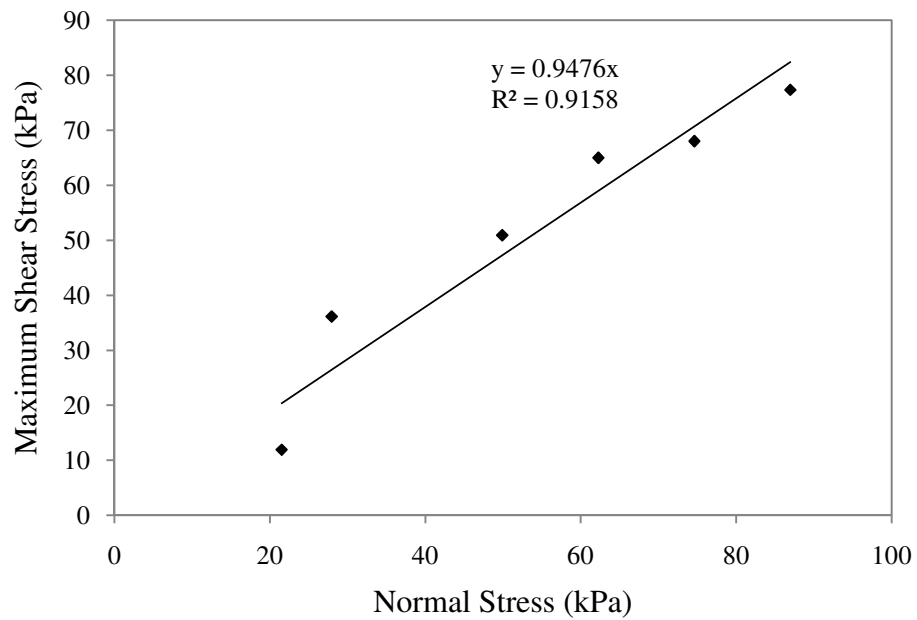
Fig. 4.11: Maximum shear stress as a function of normal stress

4.5 Drawbar Pull Comparison with Bekker's Model

In this section, Bekker's rigid wheel-deformable terrain model is used to compare the experimental drawbar pull for three sizes of wheel diameters. For each wheel size, the variables associated with Bekker's model were: wheel width, wheel diameter and total wheel load. Fig. 4.12 (a, b) and Fig. 4.13 (a, b) show the experimental and theoretical graphs of normalized drawbar pull versus total wheel load for the small scale wheels; 5" and 8" diameters iRing and Rubber wheels, respectively. As it is seen from both figures, (Fig. 4.12 and Fig. 4.13), the red curve from Bekker's model has the same trend as the experimental results, shown by the blue curves. However, the theoretical model has lower normalized drawbar pull values than the experimental results. The difference in normalized drawbar pull is about 100 N/m. One of the reasons for the different values obtained by the model from the experimental curves could be that the general theoretical model does not evaluate the wheel performance under the exact testing environment and the possible losses and forces generated by the rovers' motor operation.

Fig. 4.14 presents the experimental and theoretical graphs of normalized drawbar pull versus total wheel load by using the Bekker model and the experimental results for the 22" diameter wheels. As seen from the graphs, Bekker model is not a parabolic curve as opposed to the experimental results; the linear Bekker model increases at much higher drawbar pull values than the experimental results. Nevertheless, the model matches with the linear part of the

experimental drawbar pull for 22" diameter wheels, al low loads. However, Bekker produced a linear model which does not reflect the experimental results.

a) 5" iRing wheel

b) 5" Rubber wheel
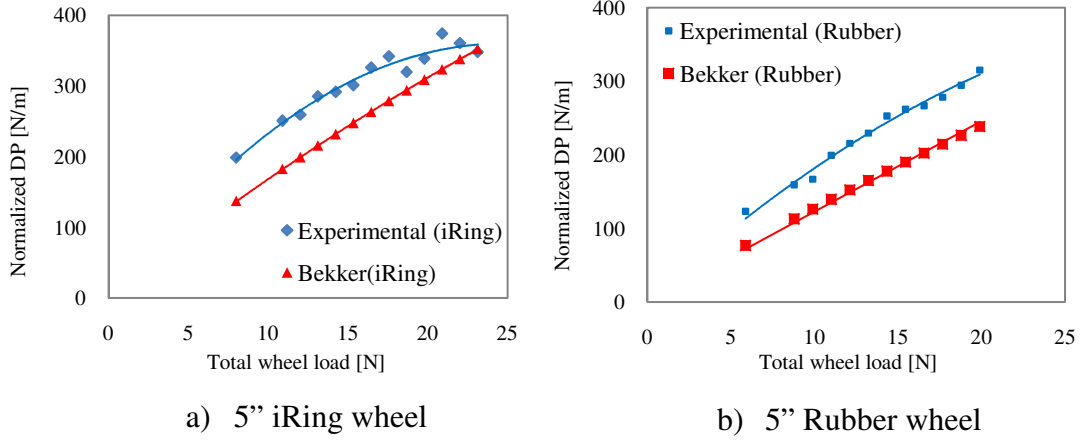
Fig. 4.12: Bekker model vs. Experiment: 5" diameter wheels. Normalized drawbar pull [N/m] as a function of total wheel load [N]

a) 8" iRing wheel

b) 8" Rubber wheel
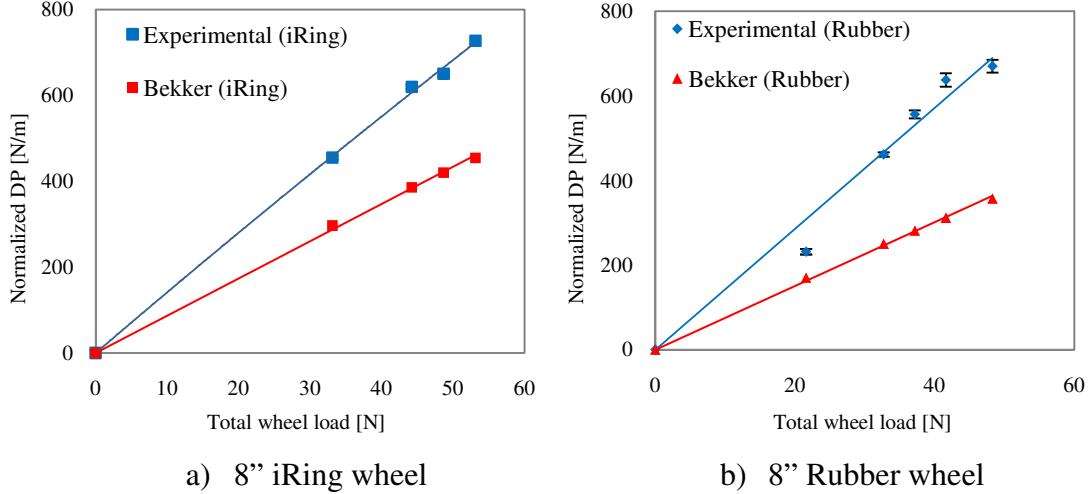
Fig. 4.13: Bekker model vs. Experiment: 8" diameter wheels. Normalized drawbar pull [N/m] as a function of total wheel load [N]
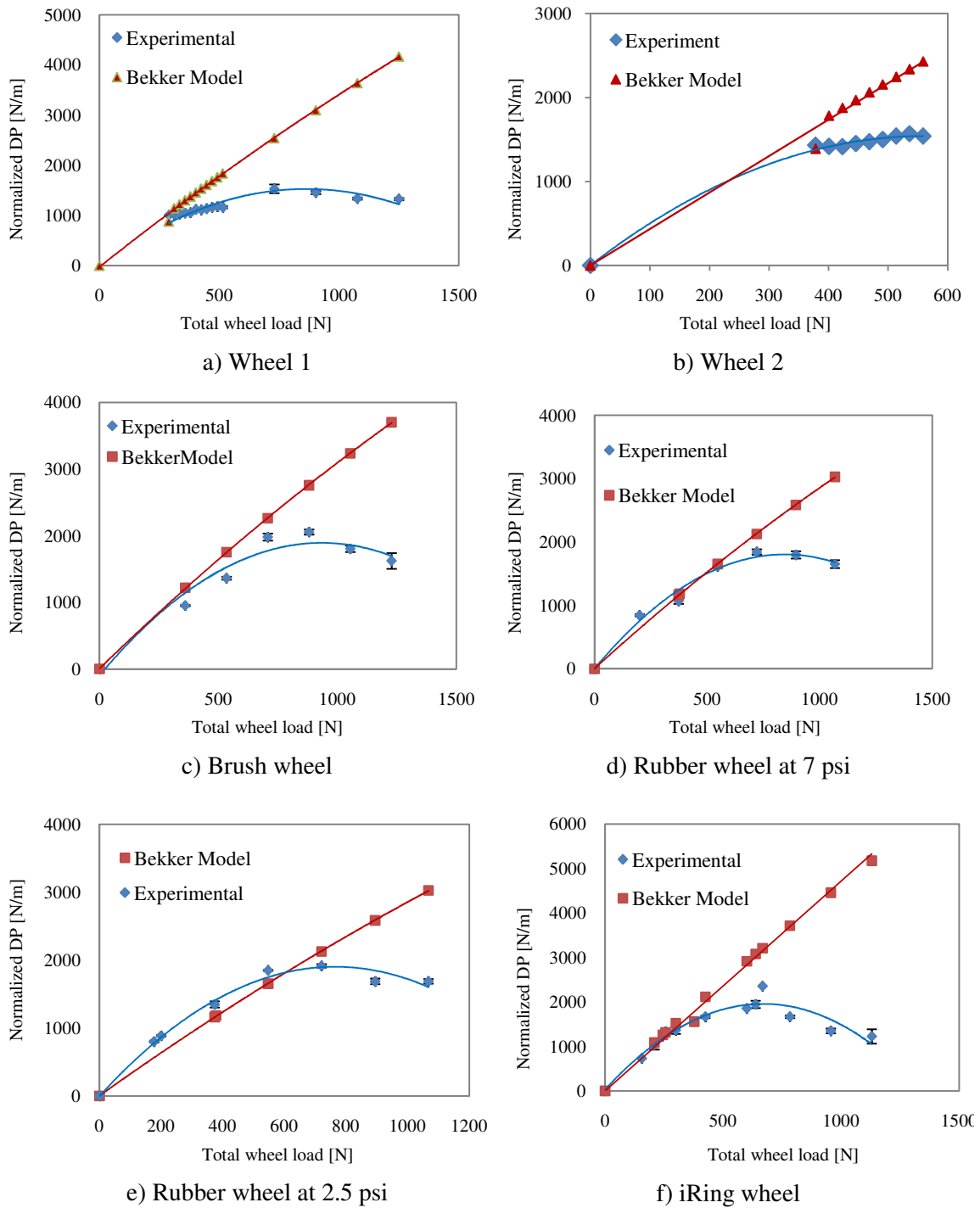
Fig. 4.14: Bekker model vs. Experiment: 22" diameter wheels. Normalized drawbar pull [N/m] as a function of total wheel load [N]

4.6 Drawbar pull comparison with Wong's model

In this section, Wong's rigid wheel-deformable terrain model has been used to generate the graphs of normalized drawbar pull versus total wheel load in order to compare with the experimental data of three sizes of wheel diameters.

In Wong's model, there are several parameters that affect the drawbar pull values. As explained in Chapter 2, in addition to soil geotechnical properties, wheel geometry, such as wheel radius and width, total wheel load and wheel entry angle (θ_1), an important variable in the evaluation of drawbar pull at very high degree of slip is the wheel exit angle (θ_2), which represents the level of soil behind the wheel. Since the experiments were performed at 100% slip, the exit angle was measured and used for the Wong model.

Fig. 4.15 shows the exit angle for each of the 22" diameter wheels at 0 and 100% wheel slip. As shown in that figure, the exit angles at 100% slip increase almost up to 3 times the exit angle at 0% slip. The accumulation of soil behind the wheel also helps to increase wheel drawbar pull; as the wheel pushes the soil surface behind it, the soil also reacts; this reaction force adds to the drawbar pull force.

To see the effect of the exit angle on drawbar pull values, graphs of the Wong model were shown for comparison with the experimental data. In each graph, from

Fig. 4.16 to Fig. 4.18, the red curve represents the Wong model at 0° exit angle, the green curve is the Wong model with the actual wheel exit angle at 100% wheel slip, as shown in Fig. 4.15, and the blue curve is the experimental data. Fig. 4.16 and Fig. 4.17 show the comparison of experimental results with Wong's model for the small scale Rubber and iRing wheels, 5" and 8" diameters respectively. As seen from these figures, with an exit angle of 0°, the Wong theoretical model generates lower drawbar pull values for both 5" and 8" diameter Rubber and iRing wheels than those obtained from the experiment. However, by giving an exit angle similar to those found for the 22" diameter Rubber at 2.5 psi and iRing wheels at 100% slip (see values in Fig. 4.15), the theoretical model matches well with the experimental data. It is clear that the exit angles measured from the 22" diameter wheels does not exactly correspond to the small scale wheels exit angle at 100% slip. Those values were used to approximate the small scale wheels exit angle, since there was not an appropriate way to adjust a camera for the small scale rovers.

Fig. 4.18 shows the comparison between Wong theoretical model and the experimental drawbar pull obtained for the six different 22" diameter wheels. The model trends for both exit angles are parabolic, similar to the trend of the experimental graphs. Once again, the drawbar pull values found with an exit angle of 0° is lower than the experimental data and lower than data found with higher exit angles. For both model curves, the location of the optimum load, where the maximum drawbar pull occurs, is shifted to higher loads than for the experimental curves.

a) Brush wheel (534 N load)
No slip
θ_2= -26.5°

Brush wheel (534 N load)
100% slip
θ_2= -57.5°
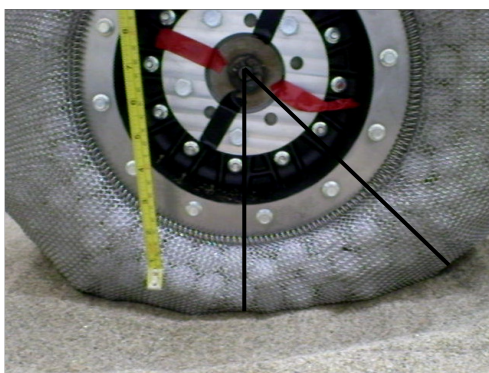
b) iRing wheel (500 N load)
no slip
θ_2= -45°

iRing wheel (500 N load)
100% slip
θ_2= -67.1
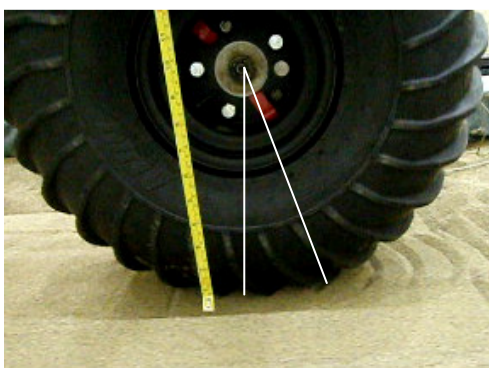
c) Rubber wheel(373 N load)
7psi (no slip)
θ_2=-23
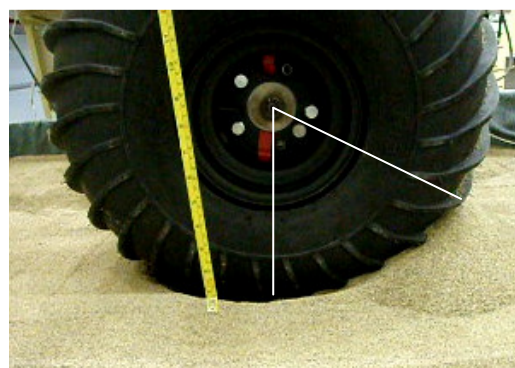
Rubber wheel (373 N load)
7psi (100% slip)
θ_2= -65

d) Rubber wheel (373 N load)
2.5 psi (no slip)
θ_2= -25.9
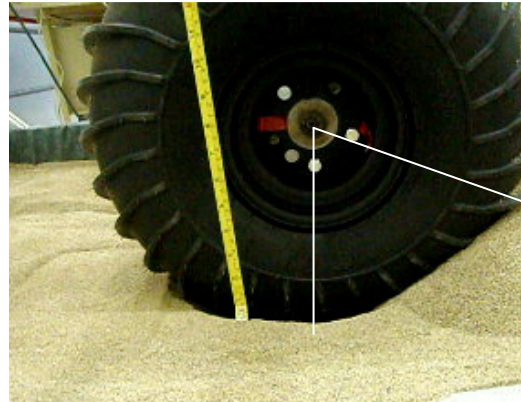
Rubber wheel (373 N load)
2.5 psi (100% slip)
θ_2= -74.0
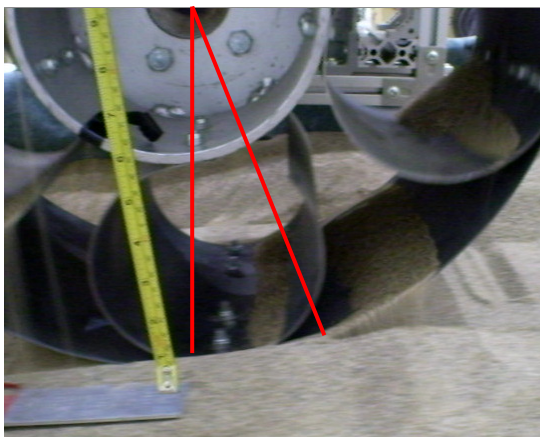
e) Wheel 1 (556 N load)
No slip
θ_2= -22.7
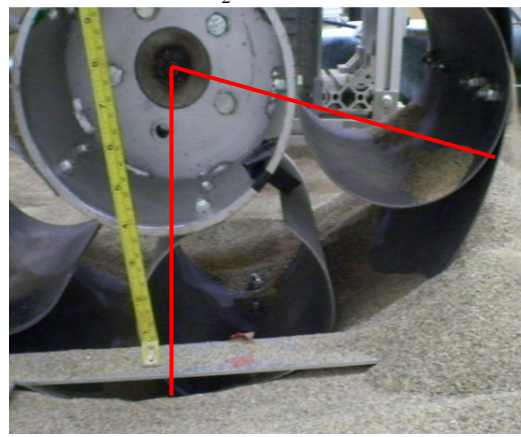
Wheel 1 (556 N load)
100% slip
θ_2= -75.2
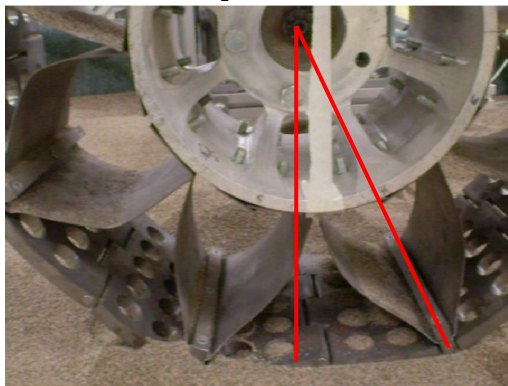
f) Wheel 2 (645 N load)
No slip
θ_2= -25.3
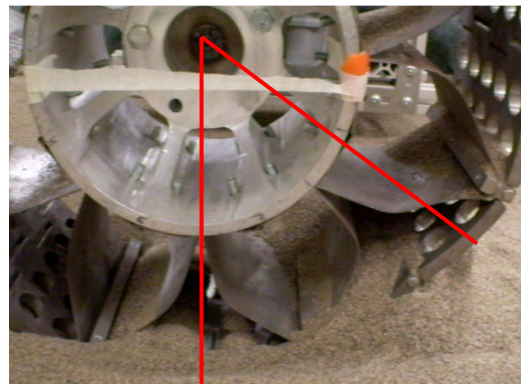
Wheel 2 (645 N load)
100% slip
θ_2= -56.3

Fig. 4.15: Exit angle (θ_2) of the 22" diameter wheels at 0 and 100% wheel slip

a) 5" Rubber wheel

b) 5" iRing wheel
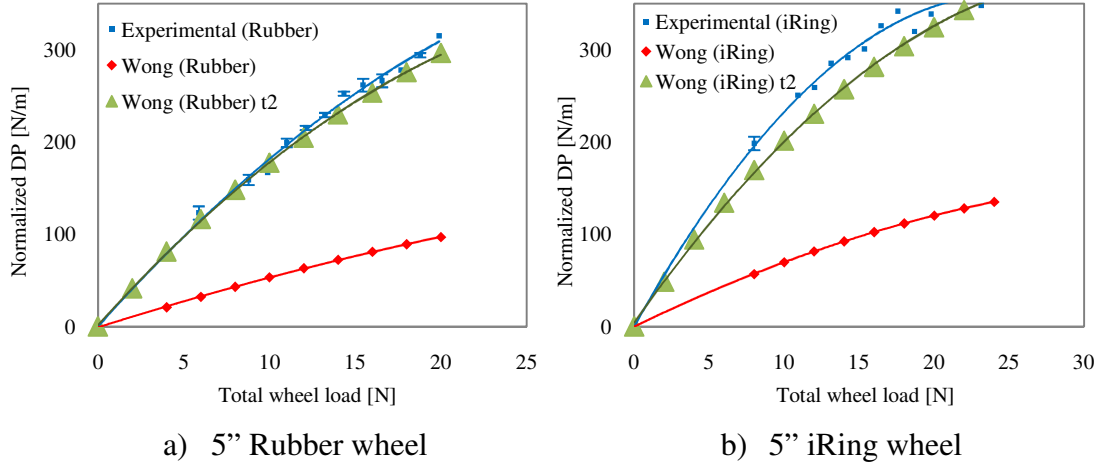
Fig. 4.16: Wong model vs. Experiment: 5" diameter wheels. Normalized drawbar pull [N/m] as a function of total wheel load [N]. (iRing t2= -67°, Rubber t2= -74°)

a) 8" Rubber wheel

b) 8" iRing wheel
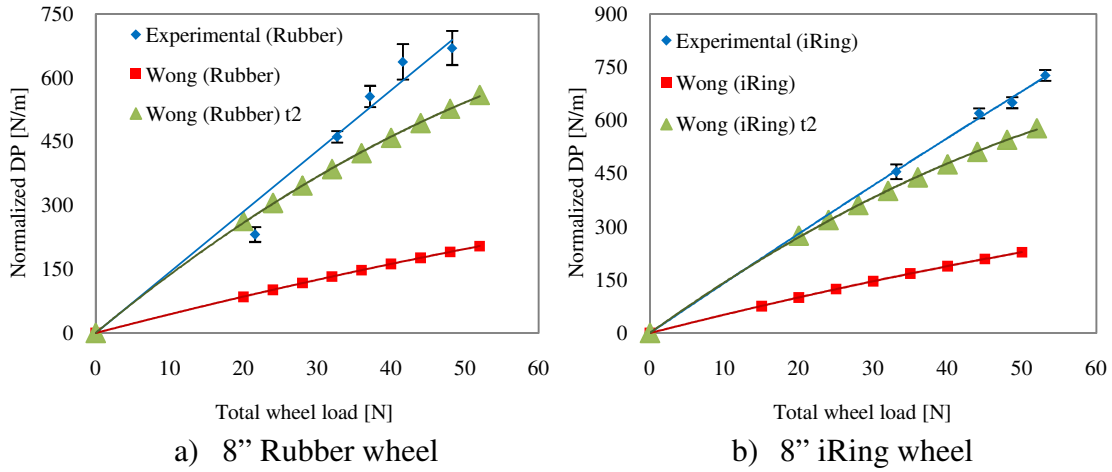
Fig. 4.17: Wong model vs. Experiment: 8" diameter wheels. Normalized drawbar pull [N/m] as a function of total wheel load [N] (iRing t2= -67°, Rubber t2= -74°)
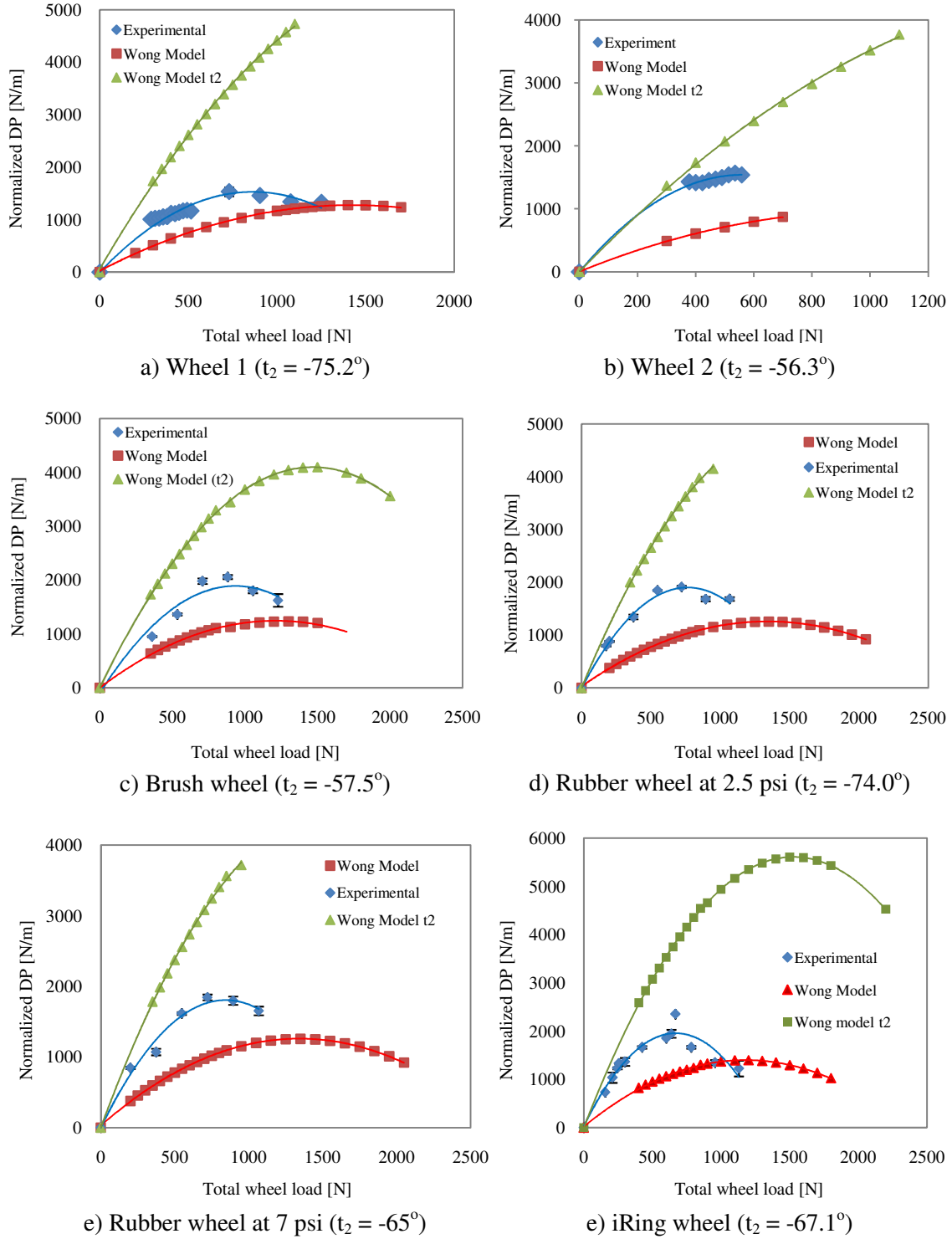
Fig. 4.18: Wong model vs. Experiment: 22" diameter wheels. Normalized drawbar pull [N/m] as a function of total wheel load [N]

81

4.7 Summary

The traction performance of three different sizes of wheel prototypes (5", 8", and 22" diameters) has been tested on dry sand using a single wheel testbed and two reduced scale rovers. Experimental results curve trend from the graphs of normalized drawbar pull to total weight matched with previous experiments from the literature.

The traction performance was measured in terms of drawbar pull as a function of total wheel load, the slope climbing ability for each wheel, wheel power consumption versus velocity and total wheel load, and the coefficient of rolling resistance. For all cases of wheel size – keeping in mind that all traction tests were completed at 100% slip – the iRing wheel showed the highest value of average drawbar pull. The 22" diameter iRing wheel achieved the highest value in maximum drawbar pull at the expense of increase in power consumption and coefficient of rolling resistance. It is expected that the efficiency of the iRings wheel is affected by the size of the particulate used, the material density used in the particulate filler, the percent filling of the chainmail tire, the tire aspect ratio and the rotation speed. As an example, the 22" wheel used was filled to about 75% of the total enveloped volume of the chainmail tire. Increasing this filling will result in a stiffer wheel and it is expected to decrease rolling resistance. The material used as the particulate was polypropylene 1" diameter solid balls with a bulk density of 0.8s.g.. However, the use of a hollow metal spheres can potentially result in bulk densities of the particulate lower than 0.5s.g. resulting in

a lower wheel mass and consequently lower rotational inertia. It is expected that the use of smaller size particulate filler will promote easier flow of the particulate which will contribute to decreasing the rolling resistance. In terms of hill climbing ability, the 22" iRing wheel had the second lowest value after Wheel 1, when compared at a load of 200N with the rest of the prototype wheels.

The 22" Rubber wheels were tested at two different pressures: 2.5 and 7 psi. The low pressure Rubber wheel showed a higher drawbar pull value than that of the higher pressure, however, the power consumption and the coefficient of rolling resistance of the 2.5 psi Rubber wheel were higher than that of the 7 psi Rubber wheel. Rubber wheel at 2.5 psi achieved the highest value for hill climbing. Rubber at 7 psi had the second highest value in hill climbing.

The 22" Brush wheel had the highest optimum weight capacity at which the maximum drawbar pull could be achieved. The maximum drawbar pull achieved by the Brush wheel was slightly smaller than the iRing wheel. Brush wheel achieved the third highest value in hill climbing ability, after Rubber wheel at 7 psi.

Wheel 2 was the heaviest prototype wheel, and its traction performance was amongst the lowest. It had the third lowest value in hill climbing. Wheel 1 had the lowest value of drawbar pull due to its smooth metal surface and the lowest hill climbing angle; however the coefficient of rolling resistance was lower than Rubber at 2.5 psi.

Soil geotechnical properties such as the internal friction angle and soil cohesion were obtained using a direct shear box apparatus. The dry sand used for the experiment had zero cohesion and relatively high internal friction angle of 43.5°.

Experimental results were compared with theory based on Bekker and Wong's rigid wheel-deformable terrain interaction models. The values obtained for the 5" and 8" wheels' drawbar pull by Bekker model were lower than those obtained from the experiment. However, for the 22" diameter wheels, none of the wheel size drawbar pull curves obtained by Bekker model was parabolic, as opposed to the parabolic fits of the experimental results. Furthermore, Bekker model showed higher drawbar pull values than the experimental data. Nevertheless, Bekker model curves matched the experimental drawbar pull at low loads for the 22" diameter wheels. In general, Bekker produced a linear model which does not reflect the experimental results.

Wong's model was obtained at two different exit angles: at 0° and at actual 22" diameter wheels' exit angle obtained experimentally at 100% slip. Exit angles increased with increasing slip, and drawbar pull values obtained with a given exit angle were higher than those obtained at no exit angles. For all three sizes of wheel diameter, the drawbar pull curves versus wheel load obtained with Wong model showed the same trend as the experimental results; however, the DP values differed for the 22" diameter. For the 5" and 8" diameter wheels, the model computed with a given exit angle matched the experimental drawbar pull values, to some extent. However, using the same exit angles, the model showed much

higher drawbar pull values and a higher optimum load than the experiment for the

22" diameter wheels.

Chapter 5

Conclusion and recommendations

In this final chapter, the objectives of the research and the methods used to achieve those goals are outlined. Significant conclusions from the experimental results are highlighted. Moreover, based on the experimental results and observations, some modifications are suggested in order to improve the testing procedure and experimental setup. Finally, future works for the improvement of the prototype wheels design are recommended.

5.1 Conclusion

The main objective of this research project was to experimentally investigate the traction performance of several prototype wheels on dry sand. The performance parameters were measured in terms of wheel drawbar pull, slope climbing ability, overall motion resistance, and power consumption. Soil geotechnical properties were also experimentally measured to evaluate the drawbar pull analytically with existing models and compare with experimental results.

To achieve the project objective, the basic theory of rigid wheel-deformable terrain interaction models was reviewed. From the theory, the important wheel performance parameters and soil geotechnical properties were understood and extracted to investigate wheel traction performance. The experimental background used for the evaluation of the performance metrics was reassessed from previous studies and employed for the purpose of this research.

The prototype wheels were regrouped in three different diameter sizes: 5", 8", and 22". The physical description of each wheel, and the experimental apparatus, as well as the testing procedures for the evaluation of their performance was carefully presented.

The traction performance of three different sizes of wheel has been tested on dry sand using a single wheel testbed and two reduced scale controllable rovers. The drawbar pull and hill climbing angle were measured at 100% wheel slip at varying normal loads; whereas power consumption and coefficient of

rolling resistance were evaluated at very low slip and low velocities with varying normal loads. Experimental results curve trend from the graphs of normalized drawbar pull to total weight matched with previous experiments from the literature. A direct shear box test was successfully used to measure soil shear stress-shear deformation parameters: internal friction angle and cohesion.

Finally, rigid wheel-deformable terrain interaction models were used to compute the analytical drawbar pull using MATLAB software and to compare with the experimental drawbar pull results.

The theoretical analysis of rigid wheel-deformable terrain interaction was based on Wong's and Bekker's models. More specifically it explained the semi-empirical equations to determine one of the most important wheel performance parameters, the drawbar pull which defines the force available to the wheel for overcoming the resistances to motion and to move the wheel forward when rolling on sand. In general, Bekker's model supposes that the normal pressure acting on the wheel with a given width is equal to normal pressure acting on a flat plate of the same width at the same depth. However, experimental results from Wong have shown that in practice, the maximum normal pressure distribution does not occur at the lowest contact point of the wheel, but rather at the intersection of the soil flows beneath the wheel which is a function of wheel slippage.

In this research, experimental results showed that for all cases of wheel size – keeping in mind that all traction tests were completed at 100% slip – the iRing wheel showed the highest value of average drawbar pull. It is expected that

the efficiency of the iRings wheel is affected by the size of the particulate used, the material density used in the particulate filler, the percent filling of the chainmail tire, the tire aspect ratio and the rotation speed. As an example, the 22" wheel used was filled to about 75% of the total enveloped volume of the chainmail tire. Increasing this filling will result in a stiffer wheel and it is expected to decrease rolling resistance. The material used as the particulate was polypropylene 1" diameter solid balls with a bulk density of 0.8s.g.. However, the use of a hollow metal spheres can potentially result in bulk densities of the particulate lower than 0.5s.g. resulting in a lower wheel mass and consequently lower rotational inertia. It is expected that the use of smaller size particulate filler will promote easier flow of the particulate which will contribute to decreasing the rolling resistance. . In terms of hill climbing ability, the 22" iRing wheel had the second lowest value after Wheel 1, when compared at a load of 200N with the rest of the prototype wheels. The 22" Rubber wheels were tested at two different pressures: 2.5 and 7 psi. The low pressure Rubber wheel showed a higher drawbar pull value than that of the higher pressure, however, the power consumption and the coefficient of rolling resistance of the 2.5 psi Rubber wheel were higher than that of the 7 psi Rubber wheel. Rubber wheel at 2.5 psi achieved the highest angle for hill climbing, and Rubber wheel at 7 psi had the second top value of hill climbing angle. The 22" Brush wheel had the highest optimum weight capacity at which the maximum drawbar pull could be achieved. The maximum drawbar pull achieved by the Brush wheel was slightly smaller than the iRing wheel. Brush wheel achieved the third highest value in hill climbing ability, after Rubber wheel at 7 psi. Wheel 2 was the heaviest prototype wheel, and its traction performance

89

was amongst the lowest. It had the third lowest value in hill climbing. Wheel 1 had the lowest value of drawbar pull due to its smooth metal surface and the lowest hill climbing angle; however the coefficient of rolling resistance was lower than Rubber at 2.5 psi.

Experimental results were compared with theory based on Bekker and Wong's rigid wheel-deformable terrain interaction models. The values obtained for the 5" and 8" wheels' drawbar pull by Bekker model were lower than those obtained from the experiment. However, for the 22" diameter wheels, none of the wheel size drawbar pull curves obtained by Bekker model were parabolic, as opposed to the parabolic fits of the experimental results. Furthermore, Bekker model showed higher drawbar pull values than the experimental data. Nevertheless, Bekker model curves matched the experimental drawbar pull at low loads for the 22" diameter wheels. In general, Bekker produced a linear model which does not reflect the experimental results. Wong's model was obtained at two different exit angles: at 0° and at actual 22" diameter wheels' exit angle obtained experimentally at 100% slip. Exit angles increased with increasing slip, and drawbar pull values obtained with a given exit angle were higher than those obtained at no exit angles. For all three sizes of wheel diameter, the drawbar pull curves versus wheel load obtained with Wong model showed the same trend as the experimental results; however, the DP values differed for the 22" diameter. For the 5" and 8" diameter wheels, the model computed with a given exit angle matched the experimental drawbar pull values, to some extent. However, using

the same exit angles, the model showed much higher drawbar pull values and a higher optimum load than the experiment for the 22" diameter wheels.

5.2 Recommendations and Future Work

In this thesis, the traction performances of each wheel – in terms of drawbar pull – were compared by evaluating the drawbar pull as the total load beneath the wheel was varied at 100% slip. The graph of drawbar pull versus load provides a reasonable understanding of the optimum load at which a wheel can achieve maximum drawbar pull values. However, it is also necessary to observe the relation of drawbar pull with variation of slips, between 0 to 100%, in order to locate the optimum value of slip where the maximum drawbar pull can be achieved by the different wheel designs. As was shown in other sections, slip is a function of wheel linear velocity and wheel angular velocity. Therefore, the use of an encoder is necessary to simultaneously measure these two variables as a function of time. Similarly, the drawbar pull can be measured instantaneously using a precise force sensor, which is available for purchase and can be attached to the wheel hub to measure the forces applied to the wheel hub. Prior to installing these instruments, the single wheel testbed must be elongated to at least twice its current length. For a controlled-slip situation, the angular velocity of the wheel is kept constant; however the carriage velocity must change in controlled way over time. Therefore, new carriage design will be required. However, for a controlled-pull technique, a new carriage design and carriage velocity change is not required, however one needs to record the slip induced from the changes of

carriage velocity due to friction on the sliders and synchronize it with force of drawbar pull.

At the present, there is a lot of friction in the polymer roller and aluminum rail, which are used to support the counterweight system. Changing the polymer roller for a steel roller and rail will help to reduce the friction.

A pressure sensor beneath the wheel, at the wheel-terrain interface, will provide more precise measurements of the actual total load and pressure distributions applied on the terrain.

Wheel contact patch and important parameters such as wheel width, contact length and contact angles could be precisely evaluated at different applied loads and during the whole wheel motion if devices such as laser measurement systems, such as the Neptec Tridar, were used.

Also, testing the wheels performance on inclined terrains could provide a better understanding of the actual wheels climbing abilities and their performance on such terrains.

From the results, it was found that in all three cases of wheel diameter, the iRing wheel prototype had the highest value of averaged drawbar pull at the cost of increase power consumption or rolling resistance. It is expected that the efficiency of the iRings wheel is affected by the size of the particulate used, the material density used in the particulate filler, the percent filling of the chainmail tire, the tire aspect ratio and the rotation speed. Therefore, future testing and development of the iRing wheel should concentrate on the impact of percent

particulate filling, the effect of ball size and the tire aspect ratio on drawbar pull, rolling resistance and power consumption.

References

Apostolopoulos, D. S. (2001). *Analytical configuration of wheeled robotic locomotion.* Pittsburgh: Carnegie Mellon University, The Robotic Institute.

Asnani, V. D. (2009). The development of wheels for the Lunar Roving Vehicle. *Journal of Terramechanics* , 89-103.

Bowles, J. E. (1979). *Physical and geotechnical properties of soils.* New York: McGraw-Hill Inc.

Briend, R., Radziszewski, P., & Pasini, D. (2010). Virtual soil calibration for wheel-soil interaction simulations using the Discrete Element Method. *CASI Astro.* Toronto.

Chu, P., Chan, S., Nguyen, C., & Vashi, S. (2009). *Compliant wheel design.* Montreal: MECH463 Mechanical Engineering, McGill University.

Costes, N. C., Farmer, J. E., & George, E. B. (December 1972). *Mobility performance of the lunar roving vehicle: terrestrial studies - Apollo 15 results.* Washington, D. C.: NASA.

Dennerlein, J., Brown, C., Kapelus, A., & Davis, S. (2009). *Lunar roving single wheel testbed.* Montreal: MECH 463 Mechanical Engineering McGill University.

Fan, T. (1985). *Multi-plate penetration tests to determine soil stiffness moduli.* Montreal: Master's Thesis McGill University.

Faragalli, M., Pasini, D., & Radziszewski, P. (2010). Performance evaluation of compliant lunar wheels in lunar soil. *61st International Astronautical Federation.* Prague: IAC.

Freitag, D. R., Green, A. J., Melzer, K. -J., & Coste, N. C. (1972). Wheels for Lunar Vehicles. *8* (3).

Freitag, D. R.-J. (1970). *Performance evaluation of wheels for lunar vehicle.* U. S. Army Engineer Waterways Experiment Station.

Gabrielli, R., St-Jean McManus, F., He, Z., & Spasojevic, M. (2009). *Compliant wheel.* Montreal: MECH463 Mechanical Engineering, McGill University.

geotechnical shear strength of soil by direct shear test. (n.d.). Retrieved 2010, from Theconstructor: http://theconstructor.org/geotechnical/shear-strength-of-soil-by-direct-shear-test/3112/

Gharib, N., & Radziszewski, P. (2010). Investigating regolith infiltration and wear of sliding surfaces. *CASI Astro.* Toronto.

Green, A. J., & Melzer, K. J. (1971). *Performance of Boeing LRV wheels in a lunar soil simulant. Report I, Effect of wheel design and soil.* US Army Waterways Experiment Station.

Head, K. (1922). *Manual of Soil Laboratory Testing.* London: Pentech Press.

Iagnemma, K., & Dubowsky, S. (2004). *Mobile robots in rough terrain: estimation, motion planning, and control with application to planetary rovers.* Springer.

Kang, S. (2003). *Terrain parameter estimation and traversability assessment for mobile robots.* Master's Thesis, Massachusetts Institute of Technology.

Karl Iagnemma, H. S. (2002). On-Line Terrain Parameter Estimation for Planetary Rovers. Proceedings of the 2002 IEEE International Conference on Robotics &Automation. Washington DC, May 2002.

Laughery, S., Gerhart, G., & Goetz, R. (1990). *Bekker's Terramechanics Model for Off-road Vehicle Research.* Warren: US Army TARDEC.

Matlab/Simulink Module AS2TM, User's Guide(2003, 2005). Hamburg: AESCO GbR.

McKyes, E. (1985). *Soil Cutting and Tillage.* New York: Elsevier.

McKyes, E., & Fan, T. (1986). Multiplate penetration tests to determine soil stiffness moduli. *Journal of Terramechanics* , 157-162.

McPherson, G. (1981). *An introduction to electrical machines and transformers.* New York: John Wiley & Sons, Inc.

Muro, T., & O'Brien, J. (2004). *Terramechanics land locomotion mechanics.* The Netherlands: Swets & Zeitlinger.

Murphy, N., & Green, A. (1969). Effects of test techniques on wheel performance. *Journal of Terramechanics* , 37 to 52.

Patel, N., & Godwin, R. (2008). Controlled soil bin tests for pneumatic tyres at heavy loads. *ASABE Annual International Meeting.* Rhode.

Patel, N., Scott, G. P., & Ellery, A. (2004). Application of Bekker theory for planetary exploration through wheeled, tracked and legged vehicle locomotion. *AIAA Space.* San Diego.

Patel, N., Slade, R., & Clemmet, J. (2010). The ExoMars rover locomotion subsystem. *Journal of terramechanics* .

Radziszewski, P., Farhat, M., Lamarche, T., Allard, P., & Dupuis, E. (2009). *Exploring lunar ATV design concepts.* Montreal: McGill University, Department of Mechanical Engineering.

Radziszewski, P., Martins, S., Faragalli, M., Kaveh-Moghaddam, N., Oyama, D., Briend, R., et al. (2010). Irings – development of a wheel prototype concept for lunar mobility. *Casi Astro 2010 Conference.* Toronto.

Sharma, A., & Pandey, K. (2001). Matching tyre size to weight, speed and power available for maximising pulling ability of agricultural tractors. *Journal of Terramechanics* , 89-97.

Taylor, B. P. (2009). *Experimental evaluation and semi-empirical modeling of the tractive performance of rigid and flexible wheels on lunar soil simulant.* Blacksburg, VA: Department of Mechanical Engineering, Virginia Polytechnique Institute and State University.

Tiwari, V., Pandey, K., & Pranav, P. (2010). A review on traction prediction equations. *Journal of Terramechanics* , 191-199.

Wilkinson, A., & DeGennaro, A. (2007). Digging and pushing lunar regolith: Classical soil mechanics and the forces needed for excavation and traction. *Journal of Terramechanics* , 133-152.

Wong, J. (2010). *Terramechanics and Off-Road Vehicle Engineering.* Ottawa: Elsevier.

Wong, J.-Y., & Reece, A. R. (1967). Prediction of wheel performance based on the analysis of soil-wheel stresses Part I. Performance of driven rigid wheel. *Journal of Terramechanics* , 81 - 98.

Appendix A

Table A. 1: Wheel-soil parameters used in Bekker and Wong models

Parameters	Symbols	Values	Units
Weight	W		N
Wheel diameter	d		m
Wheel radius	r		m
Wheel width	b		m
Wheel contact length	L		m
Wheel slip	i		%
Wheel speed	v		m/s
Wheel angular velocity	ω		rad/s
Soil internal friction angle	φ	43.5	degree
Soil cohesion		0	Pa
Shear defromation slip modulus	K	0.018	m
Modulus of soil deformation due to sinkage	k	$k_c/b+k\varphi$	Pa/m
Soil exponent	n	1	1
Modulus of friction of soil deformation	k_φ	820000	Pa/m^n
	k_c	1400	$Pa/m^{(n-1)}$
Coefficient of passive earth pressure	N_c	1.5	1
Coefficient of passive earth pressure	N_γ	25	1
Soil specific mass	γ	1680	kg/m^3
Coefficients for determining the relative position of maximum radial stress	c_1	0.43	1
	c_2	0.32	1

(Muro and O'Brien, 2004; Wilkinson and DeGennaro, 2007; Radziszewski, et al., 2009; Faragalli, Pasini, & Radziszewski, 2010)

Wong model MATLAB mfile code

```matlab
% the following m-file calculates teta for a given weight and
plots the value of teta over weight
clear;
clc;
%%%%%%%%%%%%parameters
k=0.018; %meter
r=(0.0254*22)/2;
b=0.255;
c1=0.43;
c2=0.32;
ii=1;
k1=0.3;
k2=820000;
n=1;
c=0;
fi=43.5*pi/180;
t2=-57*pi/180; %exit angle (rad)
%%%%%%%%%%%%%%%%%%%%%%%%%

weight=[300:100:1100]

alf=(k1+k2*b)*(r/b)^n;
bet=(c1+c2*ii);
for j=1:length(weight)


%%%%%%%%%%%%%%%%%%%%%%%%%%%%%%%%%%%%%%%%%%%%%%%%%%%%%%%%%%%%%%%%%%%
%%%%%%%%%%%%%%this secton estimates teta for each
weight%%%%%%%%%%%%%

          teta1=[15:0.005:90]; % the range of the guess for
teta1
          tr=pi/180*teta1;  % radian conversion
          w=weight(j); % this is the weight for which teta will
be calculated


          i=0;
          w1=0;
                  while abs(w-w1)> 0.3,
                  i=i+1;
                  t1=tr(i);
                  Q1 = quad(@(x)(r*b*alf.*(cos(x)-
cos(t1)).^n.*cos(x)),(c1+c2*ii)*t1,t1);
                  Q2=  quad(@(x)(r*b*alf.*(cos(t1-((-t2+x).*(t1-
bet*t1)/(bet*t1-t2)))-cos(t1)).^n.*cos(x)),t2,(c1+c2*ii)*t1);
                  Q3=  quad(@(x)(r*b*((c+alf.*(cos(x)-
cos(t1)).^n.*tan(fi)).*(1-exp(-r/k.*((t1-x)-(1-ii).*(sin(t1)-
sin(x)))))).*sin(x))),(c1+c2*ii)*t1,t1);
                  Q4=  quad(@(x)(r*b*(c+alf.*(cos(t1-((-
t2+x).*(t1-bet*t1)/(bet*t1-t2)))-cos(t1)).^n.*tan(fi)).*(1-exp(-
r/k.*((t1-x)-(1-ii).*(sin(t1)-
sin(x)))))).*sin(x)),t2,(c1+c2*ii)*t1);
```

```
                    w1=Q1+Q2+Q3+Q4;
                    error=abs(w-w1);
                    end


            %error
            %w1
            %w
            %t1
            angle(j)=t1*180/pi;
%%%%%%%%%%%%%%%%%%%%%%%%%%%%%%%%%%%%%%%%%%%%%%%%%%%%%%%%%%%%%%%%%%


end


    %plot(weight,angle)



%%%%%%%%%%% this section caluclates the value of drawbarpull with
respect to different weights
%
clear t1;
clear drawbarpull;
for nn=1:length(angle)
                    t1=angle(nn)*pi/180
                    Q11=  quad(@(x)(r*b*((c+alf.*(cos(x)-
cos(t1)).^n.*tan(fi)).*(1-exp(-r/k.*((t1-x)-(1-ii).*(sin(t1)-
sin(x))))).*cos(x))),(c1+c2*ii)*t1,t1)
                    Q21=  quad(@(x)(r*b*(c+alf.*(cos(t1-((-
t2+x).*(t1-bet*t1)/(bet*t1-t2)))-cos(t1)).^n.*tan(fi)).*(1-exp(-
r/k.*((t1-x)-(1-ii).*(sin(t1)-
sin(x))))).*cos(x)),t2,(c1+c2*ii)*t1)
                    Q31=  quad(@(x)(r*b*alf.*(cos(x)-
cos(t1)).^n.*sin(x)),(c1+c2*ii)*t1,t1)
                    Q41=  quad(@(x)(r*b*alf.*(cos(t1-((-
t2+x).*(t1-bet*t1)/(bet*t1-t2)))-
cos(t1)).^n.*sin(x)),t2,(c1+c2*ii)*t1)
                    drawbarpull(nn)=Q11+Q21-Q31-Q41
end
figure
plot(weight(1:length(angle)),drawbarpull/b)
```